Zhan *et al. Miner Miner Mater* 2022;1:5
DOI: 10.20517/mmm.2022.04

Minerals and Mineral Materials

Review

Open Access

Preparation and application of 0D, 2D and 3D molybdenite: a review

Weiquan Zhan[1], Yuan Yuan[1], Chang Liu[2,3], Peng Chen[2,3], Yumeng Liang[2,3], Yu Wang[2,3], José Luis Arauz-Lara[1], Feifei Jia[2,3]

[1]Instituto de Fisica, Universidad Autonoma de San Luis Potosi, San Luis Potosi, S.L.P., C.P. 78290, Mexico.
[2]School of Resources and Environmental Engineering, Wuhan University of Technology, Wuhan 430070, Hubei, China.
[3]Hubei Key Laboratory of Mineral Resources Processing and Environment, Wuhan University of Technology, Wuhan 430070, Hubei, China.

Correspondence to: Prof./Dr. Feifei Jia, School of Resources and Environmental Engineering, Wuhan University of Technology, 122 Luoshi Road, Wuhan 430070, Hubei, China. E-mail: feifeijia@whut.edu.cn

How to cite this article: Zhan W, Yuan Y, Liu C, Chen P, Liang Y, Wang Y, Arauz-Lara JL, Jia F. Preparation and application of 0D, 2D and 3D molybdenite: a review. *Miner Miner Mater* 2022;1:5. https://dx.doi.org/10.20517/mmm.2022.04

Received: 9 Mar 2022 **First Decision:** 1 Apr 2022 **Revised:** 5 Apr 2022 **Accepted:** 20 Apr 2022 **Published:** 7 May 2022

Academic Editor: Yanbai Shen **Copy Editor:** Jia-Xin Zhang **Production Editor:** Jia-Xin Zhang

Abstract

Molybdenite (MoS_2) has been widely used in the fields of catalysis, desalination, energy storage and conversion and optoelectronics as a result of its unique crystal structures and unusual properties. In the last decade, the modification of the surface, structural and semiconducting properties of zero-, two- and three-dimensional (0D, 2D and 3D) MoS_2 for enhanced applications has attracted considerable attention. In this review, we summarize the synthesis, modification methods and application of 0D, 2D and 3D MoS_2. The unique structures and properties of 0D, 2D and 3D MoS_2 are first introduced. Next, the preparation methods of 0D, 2D and 3D MoS_2 are summarized. The modification methods, including surface, structural and composite engineering, for enhancing the physical and chemical properties of 0D, 2D and 3D are also discussed. Finally, inspired by natural and modified MoS_2, future suggestions for the design of novel 0D, 2D and 3D MoS_2 for various applications are also suggested. This review offers new insights into the design and construction of novel and efficient 0D, 2D and 3D MoS_2 for practical applications.

Keywords: Zero-, two- and three-dimensional molybdenite (0D, 2D and 3D MoS_2), preparation, modification, application

INTRODUCTION

Recently, molybdenite (MoS_2), as a typical layered transition-metal dichalcogenide with unique crystal structures and unusual properties, has attracted increasing interest[1]. In the structures of MoS_2 [Figure 1A][2], strong covalent bonds exist between the Mo and S atoms and weak Van der Waals forces connect the layers. The interval distance between adjacent layers is 0.65 nm[3,4]. The Mo-S bond length, crystal lattice constant and distance between the upper and lower sulfur atoms are 0.24, 0.32 and 0.31 nm, respectively. To date, MoS_2 has been found to possess three crystal structures, namely, 1T (tetragonal symmetry, each repeat unit with one layer), 2H (hexagonal symmetry, each repeat unit with two layers) and 3R (rhombohedral, each repeat unit with three layers), according to the coordination mode between the Mo and S atoms and the stacking order between layers, as shown in Figure 1B[5]. Among these structures, 2H-MoS_2 is the most stable under normal conditions[6].

Because of its unique physical, chemical and electrical properties, MoS_2 has been researched in various fields, including desalination, energy storage and conversion, lithium and sodium batteries, biology, optoelectronics and nanodevices. So far, many works have been carried out to regulate the structure of MoS_2 for the enhancement of its performance based on different dimensional morphologies[7]. However, owing to the drawbacks of MoS_2, which include a lack of active sites, hydrophobicity and a slow transfer of photoelectrons, it must be modified with regards to its surface, structural and semiconducting properties for enhanced applications. In this review, we introduce the methods for the preparation and structural engineering of zero-, two- and three-dimensional (0D, 2D and 3D) MoS_2. Simultaneously, the perspectives of 0D, 2D and 3D MoS_2 are proposed in different application fields to provide vital guidance for researchers.

STRUCTURAL PROPERTIES

0D MoS_2

MoS_2 has a layered S-Mo-S structure and weak Van der Waals forces between the layers and can therefore form a 0D structure. The size of 0D MoS_2 is less than 10 nm and is very small in three dimensions, similar to a point. Due to the quantum limitation and small size effects, 0D MoS_2 exhibits a direct band gap, which endows it with high quantum efficiency, in contrast to bulk MoS_2 with an indirect band gap. 0D MoS_2 is considered a promising new material with low toxicity and good biocompatibility that can be used as a cell penetration probe and in vitro imaging and fluorescence sensing.

Photoluminescence

Compared with the quenching properties of MoS_2[8], one of the most promising properties of 0D MoS_2 is photoluminescence (PL). The PL emission spectra of 0D MoS_2 are at different excitation wavelengths (320-520 nm) compared with that of bulk MoS_2[9]. With a change in excitation wavelength, the emission wavelength also changes, exhibiting an excitation wavelength-dependent effect. Fluorescence microscopy images of dried 0D MoS_2 at 405, 488 and 552 nm show that 0D MoS_2 emits blue, green and red light, respectively.

In addition, there exist some relationships between the PL intensity of 0D MoS_2 and pH. For example, 0D MoS_2 synthesized by Wang *et al.*[10] showed that its PL is almost unaffected by pH. However, the PL of 0D MoS_2 synthesized by Dai *et al.*[11] was basically influenced by pH. At pH 2-6, the PL of 0D MoS_2 increases with increasing pH. However, the PL decreases with increasing pH without the movement of the peak at pH 10-12. Interestingly, Siddiqui *et al.*[12] prepared 0D MoS_2 with excitation wavelength independence. When the excitation wavelength varied from 260 to 350 nm, the emission wavelength was 448 nm.

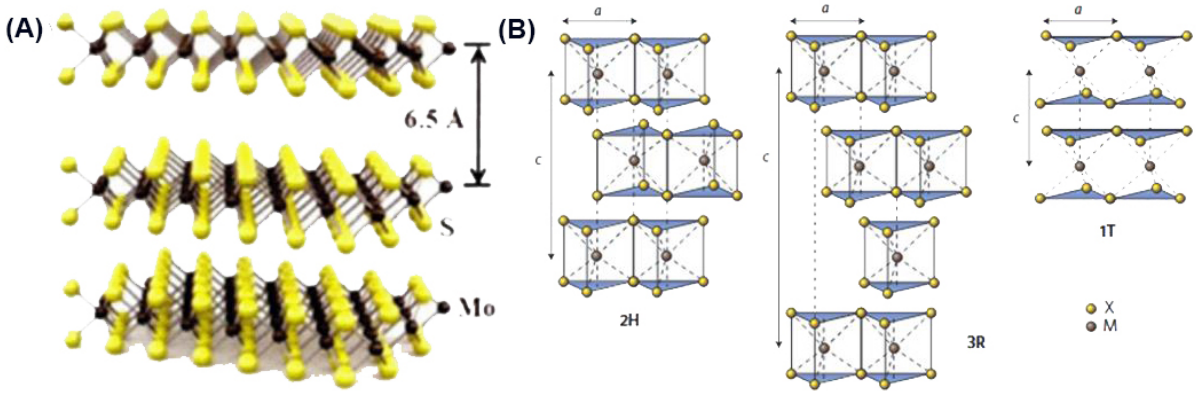

Figure 1. Layered structure of bulk MoS_2 (A)[2] and its three crystal structures: 2H; 3R; 1T (B)[5].

Anti-Stokes luminescence

Anti-Stokes luminescence is a short wavelength and high frequency light excited from long wavelength, low frequency excitation light. Dong *et al.*[13] reported the anti-Stokes luminescence properties of 0D MoS_2 in the wavelength range of 775-900 nm. When the excitation wavelength changed from 775 to 900 nm, the corresponding emission peak moved from 525 to 610 nm.

Cytotoxicity

Since 0D MoS_2 can be easily dispersed in water and exhibits strong fluorescence properties, concerns have been raised regarding its cytotoxicity. For instance, Xu *et al.*[14] used the MTT method to detect the cytotoxicity of 0D MoS_2 and HEK 293T and HeLa cells with different concentrations of 0D MoS_2 were incubated for 24 h to conduct cell survival experiments. The results showed that the survival rate of the HEK 293T and HeLa cells decreased by ~1% and ~11%, respectively, when the concentration of 0D MoS_2 was 250 μg/mL. When the concentration of 0D MoS_2 was increased to 2000 μg/mL, the cell survival rate of HEK 293T cells decreased by ~12% and that of HeLa cells by ~30%, revealing that 0D MoS_2 was harmless to the cells. The results showed better biocompatibility compared to the cytotoxicity of MoS_2 reported by Wang *et al.*[15] and also indicated the potential application value of 0D MoS_2 in the field of bioimaging.

Electrochemical activity

Recently, researchers have attempted to explore the high catalytic behavior of 0D MoS_2 in the hydrogen evolution reaction. Qiao *et al.*[16] synthesized 0D MoS_2 via multiple lithium intercalation and stripping and then tested its electrocatalytic activity using 0.5 M H_2SO_4 as an electrolyte in a typical three-electrode system. The results showed that 0D MoS_2 prepared with more stripping cycles had a lower overpotential, higher cathode current and lower Tafel slope. The reason for this was the existence of the rich active edge of 0D MoS_2 that endows it with excellent catalytic performance, thereby representing a new method for the application of 0D MoS_2 in electrochemistry.

2D MoS_2

2D layered materials refer to planar materials at the nanoscale in only one direction. These materials have transverse dimensions larger than 100 nm and can be several microns or more but are only one or a few atomic layers thick[17]. 2D MoS_2 is a representative transition metal sulfide and has attracted extensive attention from researchers. Single- or few-layer crystals of MoS_2 can be obtained by interlayer stripping because of the weak Van der Waals forces between adjacent layers. Like graphene, the transformation of MoS_2 from the bulk phase to a 2D layered structure produces some special physicochemical properties, such

as unique mechanical and electrical properties and band gap tunable fluorescence luminescence properties. It has been widely used in dry lubrication, catalysis, photovoltaic equipment and energy applications.

Electronic structure

MoS_2 is a unique layered transition metal sulfide and its band gap varies with the number of layers. The direct band gap of bulk MoS_2 is ~1.29 eV[18]. Due to its ultrathin 2D crystal structure, the band structure and band gap of MoS_2 are affected by the quantum local effect[19]. The highest valence band (VB) is at the Γ point and the lowest conduction band (CB) is about half of the Γ-K direction, which causes the transition from an indirect to direct band gap[20]. As the number of layers decreases, the lowest band in the CB rises, thereby increasing the overall bandwidth. The K point in the Brillouin region is mainly due to the fact that the d orbital of the Mo atom is not affected by the interlayer interaction. The direct band gap only increases by ~0.05-0.10 eV at the K point in the Brillouin region[21]. The CB state near the Γ point is caused by the interlayer interaction between the P_z orbital of the S atom and the d orbital of the Mo atom. Therefore, the band gap is more susceptible to the layer number change at the Γ point[22]. When the number of layers becomes one (i.e., a single layer), the indirect conversion band gap is larger than the direct conversion band gap and the minimum direct band gap is ~1.9 eV at the K point. This special transition from indirect to direct band gap originates from the interlayer influence and quantum local and long-range Coulombic effects[23].

Optical properties

Photoexcited optical studies show that monolayer MoS_2 has a very high quantum yield with a photoconversion band gap of ~1.9 eV. Compared with bulk MoS_2, the quantum yield of 2D MoS_2 is very high at 4×10^{-3}[20]. Thus, photoemission and Raman spectroscopy can be used to characterize the quality and crystallinity of 2D MoS_2[24]. The photoemission spectrum of 2D MoS_2 has two exciton peaks at the K point, namely, the exciton A peak and exciton B peak, which may be caused by the spin orbit splitting of VB. VB splitting occurs at the K point, the highest point in the VB. Therefore, two conversions from excitons to the double degenerate CB are possible[25]. 2D MoS_2 possesses higher mechanical strength and Young's modulus than steel[26]. The distortion of 2D MoS_2 can reach 11% without rupture[27]. In addition, 2D MoS_2 exhibits piezoelectricity and can be used in sensitive sensors[28]. Theoretical calculations have shown that the effective electron mass of 2D MoS_2 at the K point is 0.48 m_e, much larger than the value of 0.012 m_e for graphene[29]. Feng *et al.*[30] created a broadband optical funnel by adjusting the tension of 2D MoS_2.

3D MoS_2

2D MoS_2 can easily aggregate and stack during use, owing to its large surface energy and small particle size. During the aggregation process, the dispersion stability and effective specific surface area are reduced. Moreover, its solid-liquid separation and recycling performance are poor. The 3D structure is an effective method to improve the performance of 2D MoS_2 and can effectively reduce its inherent stacking and aggregation characteristics, thereby enhancing its specific surface area, reducing its ion diffusion resistance and increasing its number of active sites[20]. Gelation is the most common method to achieve the 3D structure of MoS_2. Through crosslinking polymerization between 2D MoS_2 and polymers, a spatial network structure with numerous pore structures and strong mechanical stability can be formed. In order to achieve the 3D structure of MoS_2, various functional groups, including carboxyl, hydroxyl and mercaptan groups and alkyl chains, can be introduced on the surface of 2D MoS_2 by organic modification[31]. A crosslinking agent is then added to make the modified 2D MoS_2 crosslinked and polymerized to form MoS_2 gel.

Characterization

Researchers have designed and constructed a series of 3D MoS_2-based materials with various frameworks (e.g., aerogels, sponges and foams). These 3D MoS_2-based materials not only retain the intrinsic properties of MoS_2 but also possess some new collective physiochemical properties, including high porosity, low density, large specific surface area, strong mechanical strength and unique electrochemical performance. Furthermore, 3D MoS_2-based materials obtain multi-level pore structures (micropores, mesopores and macropores) and internal connection frameworks, which endow them with improved surface accessibility and better mass transport.

Zhang *et al.*[31] prepared a MoS_2/graphene foam using nickel foam as a template. Nickel foam itself is a porous, microporous structure and the MoS_2/graphene obtained by this method has a large specific surface area with a Tafel slope of only 42.8 mV/decade. The existence of the 3D structure not only promotes the electron transfer process but also effectively avoids the volume change of the electrode for long periods in electrocatalytic hydrogen evolution, thereby enhancing the stability of the electrode. Liu *et al.*[32] synthesized a MoS_2/graphene hydrogel via a one-step hydrothermal method, which confirmed the existence of a microporous structure by scanning electron microscope (SEM) and specific surface area test, and directly used the prepared material as the electrode for an electrocatalytic hydrogen evolution reaction. The electrochemical experiments showed that MoS_2 has a lower initial potential and Tafel slope and its current density reached 52.4 A/g at a potential of 400 mV.

PREPARATION OF 0D, 2D AND 3D MOS_2

Synthesis of 0D MoS_2

0D MoS_2 has received extensive attention because of its unique optical properties and broad application prospects[33]. So far, the mainstream synthesis techniques of 0D MoS_2 have developed into liquid exfoliation, electrochemical, Li^+ intercalation and hydrothermal synthesis.

Liquid exfoliation method

The liquid exfoliation method uses ultrasonication to disperse bulk MoS_2 in an organic solvent and ultrasonically treat the suspension. During the ultrasonication process, MoS_2 is damaged and sheared into small sizes by mechanical force[34]. The choice of solvent is particularly important because the solubility and surface tension index of the solvent are related to the good monodispersity[35]. Gopalakrishnan *et al.*[36] subjected a MoS_2 powder to bath sonication and probe sonication in sequence for 3.5 h in a 1-methyl-2-pyrrolidone (NMP) solution and then centrifuged it to obtain heterodimensional nanostructures on the upper layer of the solvent, as shown in Figure 2. In bath sonication, the hydrodynamic forces generated by the increase in pressure and temperature promoted the cleavage of bulk MoS_2 into small particles. Probe sonication broke most of the nanosheets into ultrathin sheets with 0D MoS_2 interspersed. The presence of NMP maintains the stability of the exfoliated MoS_2 dispersion the highest. This method yielded ~2 nm single-layer 0D MoS_2, which slightly agglomerated over time and could become 10 nm after 7 d. Another commonly used solvent is N,N-dimethylformamide (DMF). Wang *et al.*[37] placed bulk MoS_2 powder in DMF and successfully prepared 0D MoS_2 of 1.47 nm ± 0.16 nm by a combination of ultrasonic exfoliation for 4 h and gradient centrifugation. Dong *et al.*[13] used TBA to insert the interlayer and ultrasonic treatment to assist in the preparation of bulk MoS_2 flakes with a lateral size of ~13 nm. The flakes were uniformly distributed with 0D MoS_2 in a honeycomb lattice atomic structure, a uniform crystal form and a height of 1-2 nm.

Electrochemical method

The electrochemical method is an environmental-friendly, efficient and condition-controllable method for

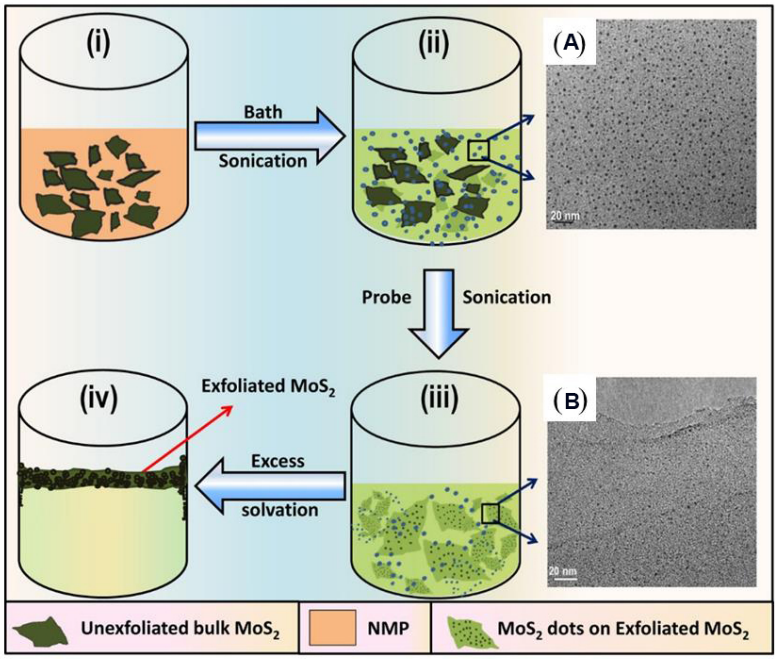

Figure 2. Schematic diagram of 0D MoS_2 synthesized by liquid exfoliation method [insets (A,B): TEM images of 0D MoS_2][36].

preparing 0D MoS_2[38,39]. A direct current (DC) voltage is applied to the electrolyte and free radicals are generated in the solution. The radicals etch MoS_2, thereby triggering its cleavage, leading to further exfoliation of the bulk material that results in monolayer or multilayer 0D MoS_2[40]. Shrivastava *et al.*[41] placed MoS_2 microspheres in a two-electrode system of an electrochemical cell with a 1 mol% lithium bis-trifluoromethylsulphonylimide ionic liquid as the electrolyte. A constant DC voltage of 5 V was applied to the electrode pair and the reaction continued for 3 h. 0D MoS_2 was separated from the supernatant after centrifugation, washed with acetone and dried at room temperature to obtain 0D MoS_2 in powder form. Li *et al.*[42] used the electro-Fenton reaction to generate a large number of hydroxyl radicals, which acted on the preparation of 0D MoS_2, as shown in Figure 3. The nanosheets could be completely converted into uniformly distributed single 0D MoS_2 by continuously applying a potential of -0.5 V and bubbling O_2 to the mixed solution containing MoS_2 nanosheets and $FeSO_4$ for 60 min. The electro-Fenton reaction can be used to easily obtain nanosheets with different nanopores, as well as 0D MoS_2, by controlling the time.

Intercalation method

Intercalation is the most suitable route for the large-scale production of monolayer MoS_2 and 0D MoS_2. By controlling the number of repeated exfoliation steps on the sample by lithium intercalation, monolayer MoS_2 nanosheets with different lateral dimensions can be generated until a large number of 0D MoS_2 monolayers with sufficiently small size can be obtained[43]. Three important mechanisms contribute to the exfoliation of MoS_2 and the preparation of 0D MoS_2: (1) the intercalation agent intercalates between the layers of the material, which weakens the interlayer force; (2) the intercalation agent reacts violently with water to generate H_2, which further increases the interlayer spacing; (3) coulombic repulsion exists between the layers[44]. Lithium-containing compounds and some alkali metal compounds can be used as intercalation agents, among which n-butyllithium (n-BuLi) is widely used for the exfoliation of layered materials. Qiao *et al.*[43] soaked MoS_2 powder in an n-BuLi solution for a long period, followed by stripping, filtration, washing, sonication and drying. The above process was repeated three times and single-layer 0D MoS_2 was finally prepared. n-BuLi easily leads to the transformation of MoS_2 from the semiconducting 2H phase to

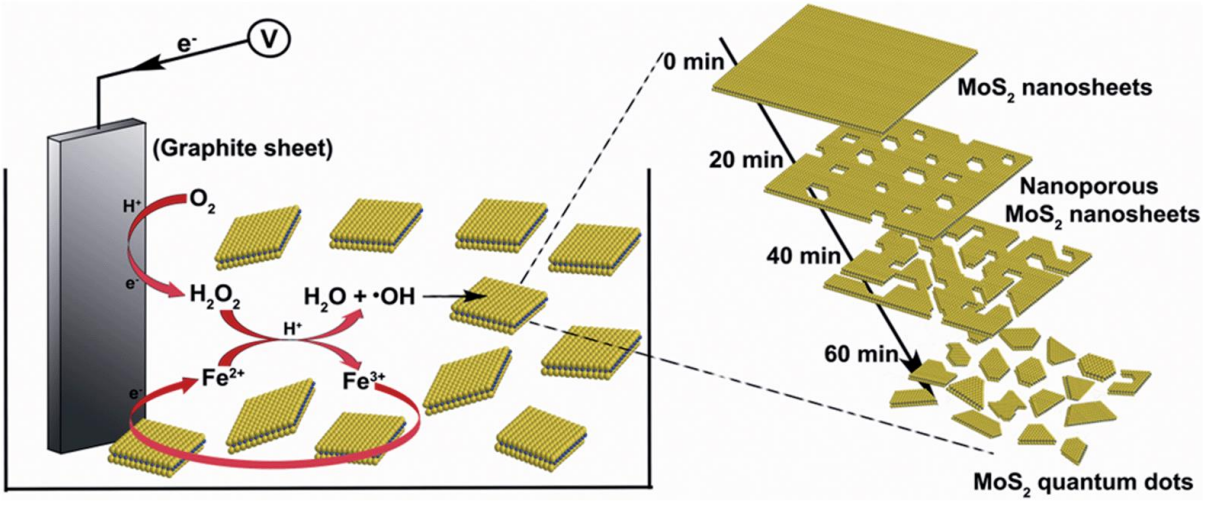

Figure 3. Schematic diagram of 0D MoS_2 synthesized by electrochemical method[42].

the metallic 1T phase during the intercalation process. An *et al.*[45] proposed the addition of laser radiation-assisted stripping on the basis of Li^+ intercalation to induce the 1T phase transition to 5-10 nm 2H phase 0D MoS_2, as shown in Figure 4. It is noteworthy that part of the MoS_2 oxidized spontaneously due to laser ablation.

Hydrothermal method

Under the premise of using water as the solvent, by placing the precursor solution in a closed reactor and controlling the reaction time, temperature, pressure and other conditions, 0D MoS_2 with different structures and morphologies can be prepared. Wang *et al.*[10] used sodium molybdate and L-cysteine as precursors and reacted them in an autoclave at 200 °C for 36 h to obtain 0D MoS_2 of ~2.5 nm in solution. Ren *et al.*[46] converted the sulfur source into dibenzyl disulfide and reacted it with $Na_2MoO_4{\cdot}2H_2O$ at 220 °C for 18 h to obtain 0D MoS_2 with a uniform distribution and an average size of 3.6 nm, as shown in Figure 5. Mohanty *et al.*[47] used ammonium tetrathiomolybdate $[(NH_4)_2MoS_4]$ as the single precursor and hydrazine hydrate ($N_2H_4{\cdot}4H_2O$) as the reducing agent and reacted them at 200 °C for 24 h to obtain 0D MoS_2 with an average size of 2.8 nm. This one-step hydrothermal synthesis avoids the inhibition of the performance of 0D MoS_2 by carbon that may be generated in the presence of organic solvents.

Synthesis of 2D MoS_2

Based on its excellent properties, significant research work has been carried out to prepare high-quality 2D MoS_2. At present, the preparation strategies for 2D MoS_2 can mainly be divided into top-down and bottom-up methods [Figure 6][48]. The basic principle of the top-down method is to reduce the interlayer force of massive MoS_2 and then prepare high-quality materials by stripping. The bottom-up method mainly uses Mo and S precursors to prepare 2D MoS_2 through chemical synthesis.

Top-down methods

Micromechanical cleavage method

Micromechanical cleavage is a traditional top-down method for preparing 2D materials. According to the Van der Waals forces between the material layers, suitable adhesive tapes can be selected for artificial stripping to prepare single- or few-layer 2D materials, including the preparation of 2D MoS_2. Li *et al.*[49]

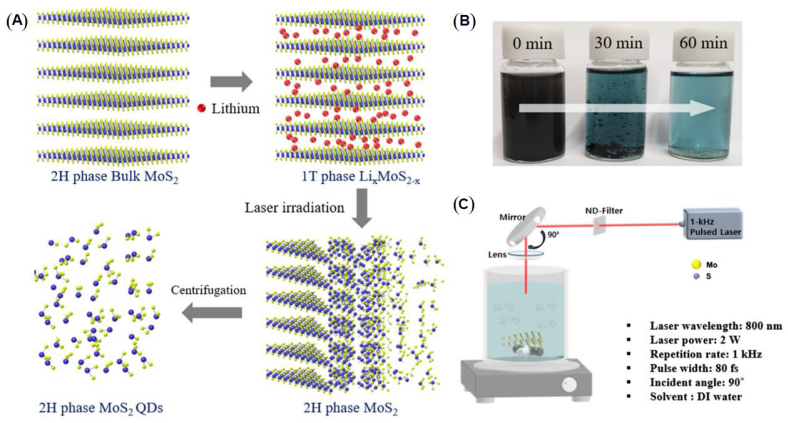

Figure 4. Schematic diagram of 0D MoS_2 synthesized by intercalation method (A). Digital images of solution change during exfoliation (B). Schematic diagram of experimental setup (C)[45].

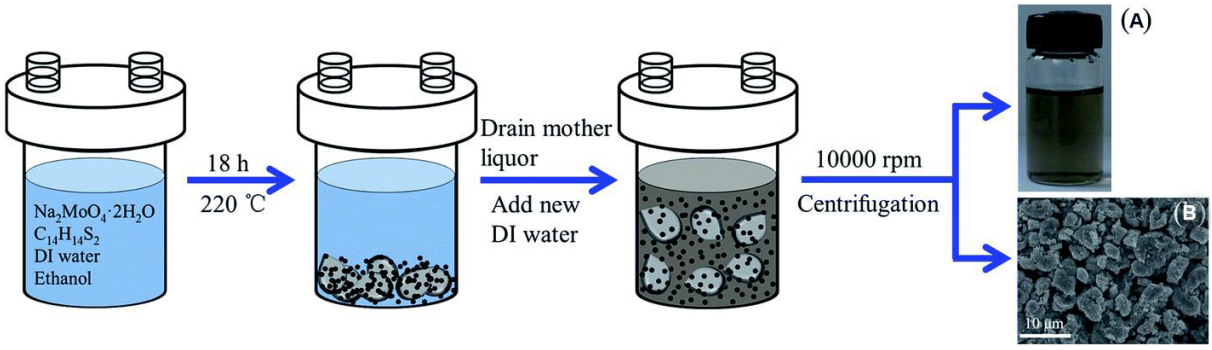

Figure 5. Schematic diagram of 0D MoS_2 synthesized by hydrothermal method. Digital image of 0D MoS_2 suspension (A). SEM image of μm-sized 0D MoS_2 (B)[46]. SEM: Scanning electron microscope.

exfoliated suitable MoS_2 from bulk crystals using Scotch tape and then contacted these newly peeled flakes on the tape with the target substrate and rubbed them with tools, such as plastic tweezers, to further cut them. After removing the Scotch tape, the obtained optical microscopy and AFM images of single- or few-layer 2D MoS_2 on the substrate are shown in Figure 7A1-8. The height of monolayer MoS_2 is ~0.8 nm, which is consistent with the theoretical value[50]. Similarly, Ghatak *et al.*[51] obtained different layers of 2D MoS_2 by tape stripping, in which schematics of optical microscopy and field-effect transistors are exhibited in Figure 7B1-2. It is obvious that the separation of the E_{2g}^1 and A_{1g} peaks for three-, two- and single-layer 2D MoS_2 are 23, 21 and 16-18 cm^{-1}, respectively, as characterized by Raman spectroscopy [Figure 7B3-4]. 2D MoS_2 obtained from Scotch tape has nearly perfect surfaces and high crystallinity and is usually used as a material for optoelectronic devices in fundamental research. Simultaneously, the high crystallinity of 2D MoS_2, which leads to its low chemical activity, reduces its application prospects in other aspects, such as photocatalysis and adsorption. In addition, the micromechanical cleavage method faces the limitations of small yield and low production efficiency. These problems limit the application of this method to fundamental research at present, and it is difficult to realize the actual production of 2D MoS_2 using this method.

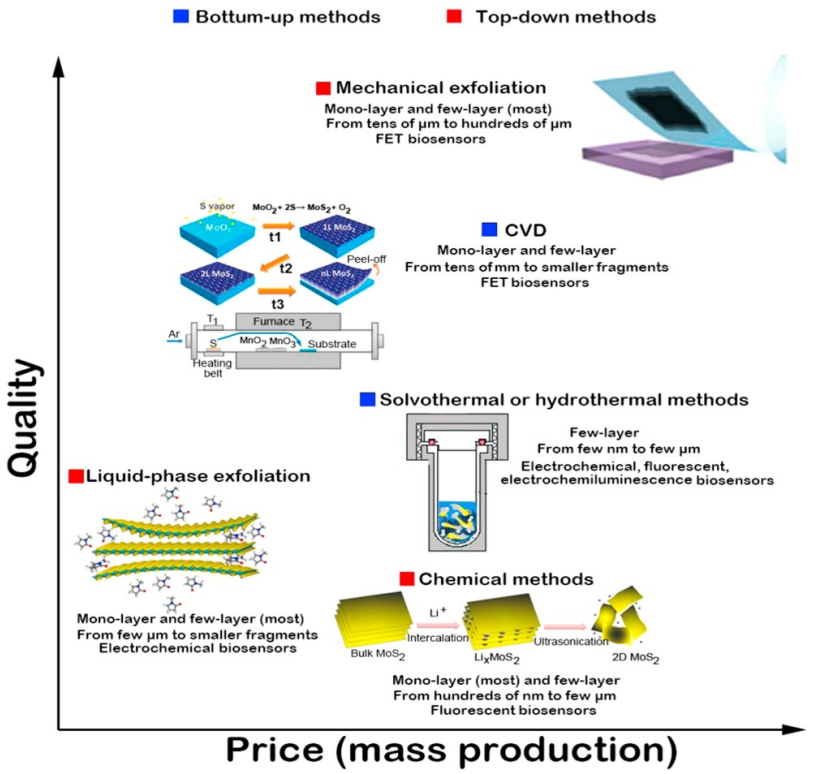

Figure 6. Preparation methods of 2D MoS_2[48].

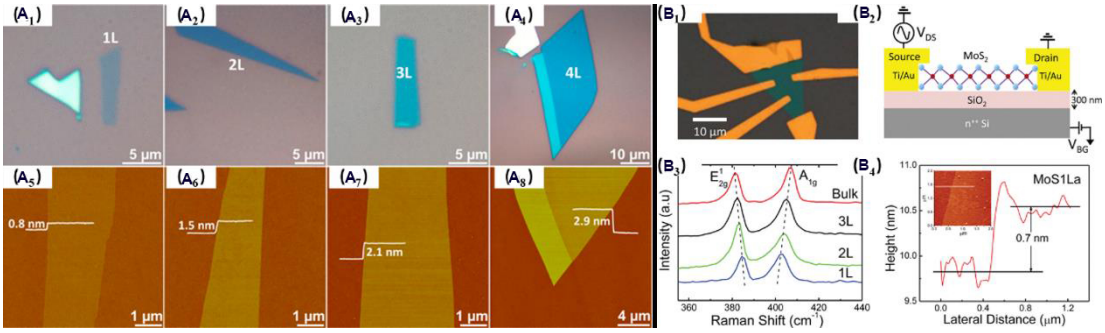

Figure 7. Mechanically exfoliated 2D MoS_2 on 300 nm SiO_2/Si: optical microscopy (A_{1-4}). AFM images (A_{5-8})[49]. Optical micrograph of a typical MoS_2 device (B_1). Schematic of a single-layer MoS_2 field-effect transistor (B_2). Raman spectrum (B_3). Thickness scan of single-layer MoS_2 (inset: AFM image) (B_4)[51].

Liquid exfoliation

The basic strategy of liquid exfoliation, similar to chemical mechanical exfoliation, is to disperse the bulk crystals in the liquid phase to reduce the interlayer force and then peel the 2D materials from the bulk and disperse them stably in the solvent by assisted shear or ultrasound. In this method, reducing the interlayer force of MoS_2 is pivotal to preparing high-quality 2D MoS_2. Therefore, significant research has been conducted on the method for effectively reducing the interlayer force of MoS_2 in recent years. According to the different methods to reduce the interlayer force, the liquid exfoliation technology of MoS_2 can be mainly divided into solvent-assisted stripping, surfactant-assisted stripping and ion intercalation stripping.

Solvent-assisted stripping, as one of the most direct methods for stripping layered materials, involves dispersing MoS_2 in an organic solvent and then performing ultrasonic stripping to finally obtain 2D MoS_2 by centrifugation. It has been shown that the energy required for stripping layered minerals is strongly related to the difference between the surface energy of layered minerals and the surface tension of the organic solvents[52]. In addition, a suitable solvent can stabilize the dispersion of 2D MoS_2 by inhibiting the agglomeration and restacking between nanosheets. In summary, the type of dispersing solvent plays a decisive role in the stripping efficiency of MoS_2 and the commonly used solvents include NMP, dimethyl sulfoxide and DMF[53]. Li *et al.*[54] successfully dispersed massive MoS_2 in an NMP solvent. The high-speed shear effect of the homogenizer was used to overcome the weak Van der Waals forces between the MoS_2 layers in NMP, which reduced the size of the sheet [Figure 8A]. From AFM images of 2D MoS_2 in the supernatant (MoS_2-p) and the histogram of layer number [Figure 8B1-2], the statistical data suggested that the thickness distribution of 2D MoS_2 was wide, while the average layer number was around six. By adding sodium citrate to the NMP suspension, the concentration of 2D MoS_2 in the supernatant (MoS_2-sc) was greatly increased and the dispersion stability was also significantly improved. More importantly, the thickness of the obtained 2D MoS_2 was thinner and the distribution narrower. The average layer number of 2D MoS_2 was about four, of which ~9% were single layers, as shown in Figure 8B3-4. Although the effective stripping of MoS_2 can be achieved by using NMP as a solvent, it is difficult to be popularized due to the toxicity of NMP. Furthermore, the removal of NMP (and other solvents) from 2D MoS_2 is also challenging.

Surfactant-assisted stripping is the other liquid exfoliation method. Small molecular organics, surfactants and polymers have high adsorption energy on the molybdenite surface, which greatly promotes its separation. The surfactants can be divided into ionic and nonionic depending on their structure. Gupta *et al.*[55] obtained stable water dispersions of 2D MoS_2 by ultrasonic treatment in the presence of cationic surfactant cetyltrimethylammonium bromide (CTAB) or anionic surfactant sodium dodecyl sulfate (SDS). Observation of the micromorphology of 2D MoS_2 stripped by CTAB revealed that it was highly dispersed and exhibited a defect-free structure and a hexagonal honeycomb shape [Figure 9A3-5]. As shown by the AFM analysis in Figure 9A2, the thickness of 2D MoS_2 was ~1.2 nm, indicating that the nanosheets in the MoS_2 dispersion were composed of one or two layers, irrespective of the surfactant used for exfoliation. Interestingly, the magnitude and distribution of the potential energy of the two dispersions [Figure 9A1] were similar, but their signs were opposite (CTAB was positive and SDS was negative). These charges must have been generated by the interaction between 2D MoS_2 and the surfactant because there were no ionizable groups on the 2D MoS_2. Guardia *et al.*[56] used a series of nonionic surfactants, including polyoxyethylene sorbitol monooleate (Tween 80), polyoxyethylene sorbitol trioleate (Tween 85), PVP, polyoxyethylene (4) dodecyl ether (Brij 30) and so on, to effectively produce h-BN [Figure 9B1,4], 2D MoS_2 and WS_2 [Figure 9B3,6] suspensions with long-term stability (several months). It was clear through AFM analysis that the produced 2D MoS_2 consisted of platelets with lateral dimensions from fifty to several hundred nanometers and thicknesses in several nanometers [Figure 9B2,5]. Unfortunately, the 2D MoS_2 dispersion obtained by this method exhibited anti-aggregation properties and its inherent characteristics were degraded to a certain extent due to the loading and modification of the surfactant.

The ions inserted between the layers can significantly reduce the Van der Waals forces between the layers of a layered material, and then the slices can be easily separated by a simple mechanical external force. Therefore, ion intercalation is considered an excellent liquid exfoliation method to improve the exfoliation efficiency of layered materials. For MoS_2, because its layer spacing is small (~0.65 nm), only Lewis or alkali metal bases with a small ionic radius can be inserted into the interlayers. At present, Li^+ intercalation stripping is the most versatile and effective method for molybdenite exfoliation, as schematically depicted in Figure 10A[57]. The method mainly includes three steps. Firstly, MoS_2 is immersed in an inert solvent

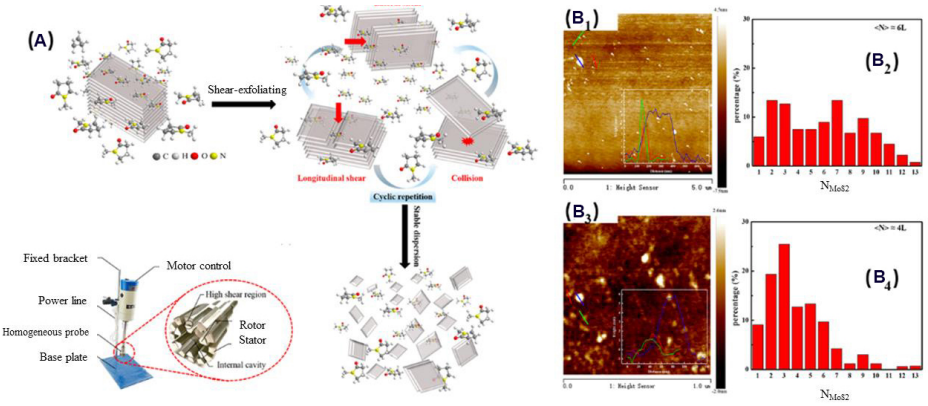

Figure 8. Schematic diagram of liquid-phase shear exfoliation of 2D MoS_2 by a high-speed dispersive homogenizer (A). Typical AFM images (left) and histogram of layer number of 2D MoS_2 calculated from height measurements of AFM images of above 100 flakes (right): MoS_2-p (B_{1-2}); MoS_2-sc (B_{3-4})[54].

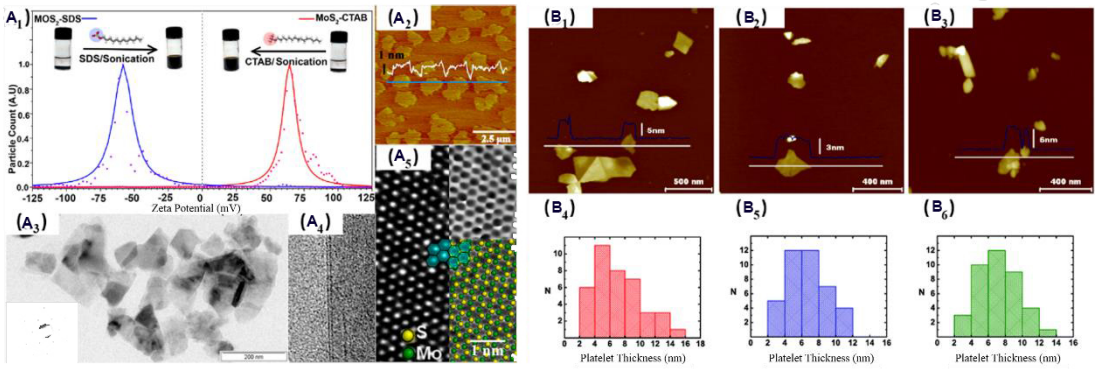

Figure 9. Digital image of MoS_2, surfactant solutions before and after sonication and the zeta potential distribution of as-prepared MoS_2-CTAB and MoS_2-SDS dispersions (A_1). Tapping-mode AFM images (the height profiles of the sheets along the blue line marked on the images are indicated in white), electron microscope images (inset: selected area diffraction pattern) and TEM and HRTEM images of MoS_2-CTAB (A_{2-5})[55]. AFM images of platelets exfoliated in water with Tween 80 and deposited onto mica substrates: h-BN (B_1); MoS_2 (B_2); WS_2 (B_3). Histogram of thickness distribution of the sample in the corresponding AFM image: h-BN (B_4); MoS_2 (B_5); WS_2 (B_6)[56].

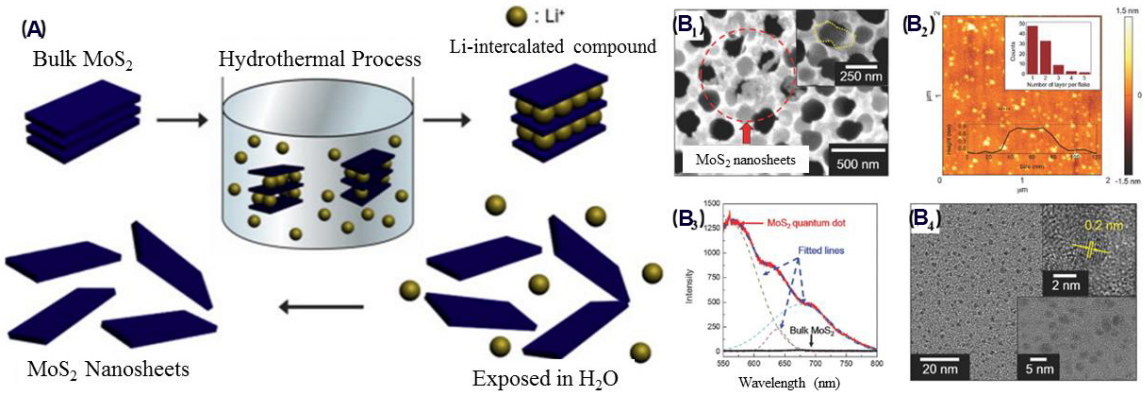

Figure 10. Schematic representation of the formation of 2D MoS_2 (A)[57]. SEM images (flakes were vacuum filtered on an aluminum oxide membrane) and AFM image of 2D MoS_2 (inset: histogram of the number of layers of 2D MoS_2 measured from AFM images) (B_{1-2}). PL spectra of bulk MoS_2 and 2D MoS_2 (B_3). TEM images of MoS_2 quantum dots (B_4)[59].

containing n-butyl lithium to promote the insertion of lithium ions into the interlayer of MoS_2. The intercalated MoS_2 is then immersed in pure water and Li_xMoS_2 is hydrolyzed rapidly to produce a large amount of hydrogen, which causes the interlayer expansion of MoS_2. Finally, 2D MoS_2 is produced by ultrasonic-assisted stripping[58]. This method is low-cost and scalable. However, n-butyl lithium is highly reductive and reacts violently with water, resulting in serious deformation of the 2D MoS_2 structure. In addition, the intercalation reaction time is particularly long, and the insertion amount of Li^+ in molybdenite cannot be effectively controlled.

Later, Yeon *et al.*[59] introduced a new strategy for exfoliating nanosheets in an environmentally-friendly and inexpensive aqueous solution using Na^+ instead of Li^+. The morphology and thickness of 2D MoS_2 exfoliated with 0.1 M Na^+ are characterized in Figure 10B1-2. The 2D MoS_2 slices are thin enough to clearly observe film holes through them, with most being monolayer or bilayer MoS_2, according to the AFM statistics. The bulk MoS_2 does not show any identifiable emission owing to its indirect band gap. In contrast, the exfoliated 2D MoS_2 has a PL peak near 650 nm, which is similar to that obtained by stripping bulk MoS_2 with Scotch tape. In addition, a strong PL peak is observed at 565 nm [Figure 10B3], which is considered to originate from MoS_2 quantum dots, similar to 0D MoS_2 observed by TEM in Figure 10B4. Similarly, the electrochemically assisted Li^+ intercalation method has been used to achieve the effective stripping of MoS_2, as described in detail in the later electrochemical stripping section.

In order to achieve green and efficient liquid exfoliation, external forces have also been developed to prepare 2D MoS_2. Usually, grinding and shearing can be used to separate layers from bulk MoS_2, thereby increasing the exfoliation yield of MoS_2 [Figure 11A]. Yu *et al.*[60] used pure water as a solvent, separated bulk MoS_2 through the mechanical force between sandpapers in a mechanical sanding machine and dispersed 2D MoS_2 in water by a cell grinder, thereby realizing this stripping process. It is found by SEM in Figure 11b1-3 that the exfoliated 2D MoS_2 is randomly stacked and the thickness of the sheet is several nanometers. Its transverse size is found to be in the range of 500 nm to 5 μm by TEM [Figure 11B4-6], which is consistent with the SEM results. Lee *et al.*[61] dispersed a MoS_2 powder using ultrasound in a water/ethanol system and obtained a 2D MoS_2 supernatant by two-step centrifugation. It was shown that almost the smallest size of MoS_2 sheet could be obtained at high centrifugal speed, with a primary height of 3-4 nm and an average height of ~7 nm through characterizing the 2D MoS_2 deposited on a Si/SiO_2 substrate by AFM. Although the stability of the obtained dispersions may not be as stable as in organic solvents, these methods can realize on-site production and avoid the use of organic solvents.

Electrochemical exfoliation

Since MoS_2 has certain semiconducting properties, 2D MoS_2 can be prepared by electrochemical expansion. You *et al.*[62] reported an environmentally-friendly electrochemical stripping method for the rapid and large-scale production of 2D MoS_2 at low cost for the first time. Schematic diagrams of the electrochemically expanded MoS_2 device are shown in Figure 12A1-2, where the bulk natural MoS_2 and platinum foil are connected to the two electrodes, respectively, and immersed in a 0.5 M H_2SO_4 aqueous solution. A potentiostat was used to apply a bias potential between MoS_2 and Pt. In the initial stage, a static bias of +1 V was applied to MoS_2 for 10 min, which was then increased to +10 V and kept constant for 30 min to complete the exfoliation process. Finally, 2D MoS_2 could be obtained by placing the expanded MoS_2 in a DMF solution and then stripping the expanded MoS_2 under ultrasonic assistance. As shown in Figure 12B1-2, the average morphology height of exfoliated MoS_2 on the Si/SiO_2 substrate measured by AFM was ~1.8 nm and the transverse size was ~10 μm. In addition, EDS scans showed only Mo, S and other four elements, indicating pure MoS_2 on the Si/SiO_2 substrate. The sharp, obvious vibration peaks in the

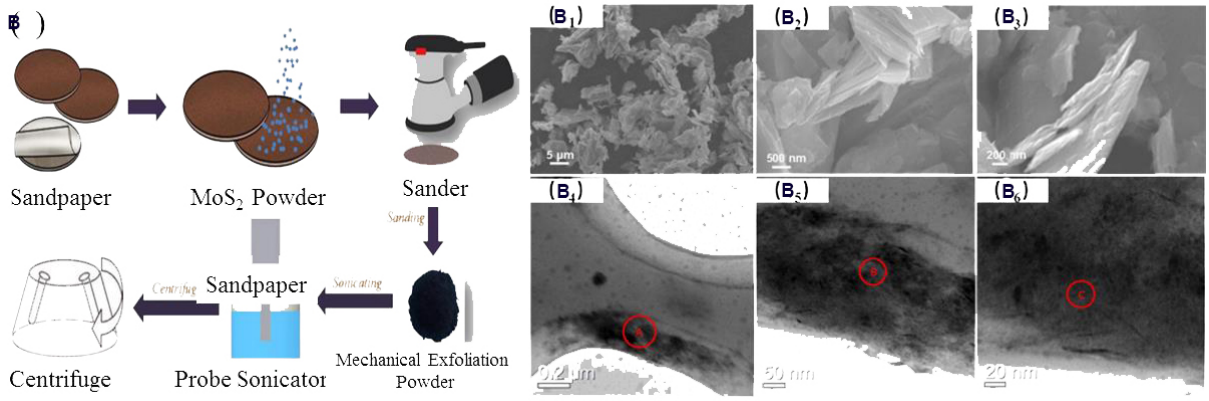

Figure 11. Typical green exfoliation process of 2D MoS_2 (A). SEM (B_{1-3}) and TEM Images (B_{4-6}) of 2D MoS_2[60].

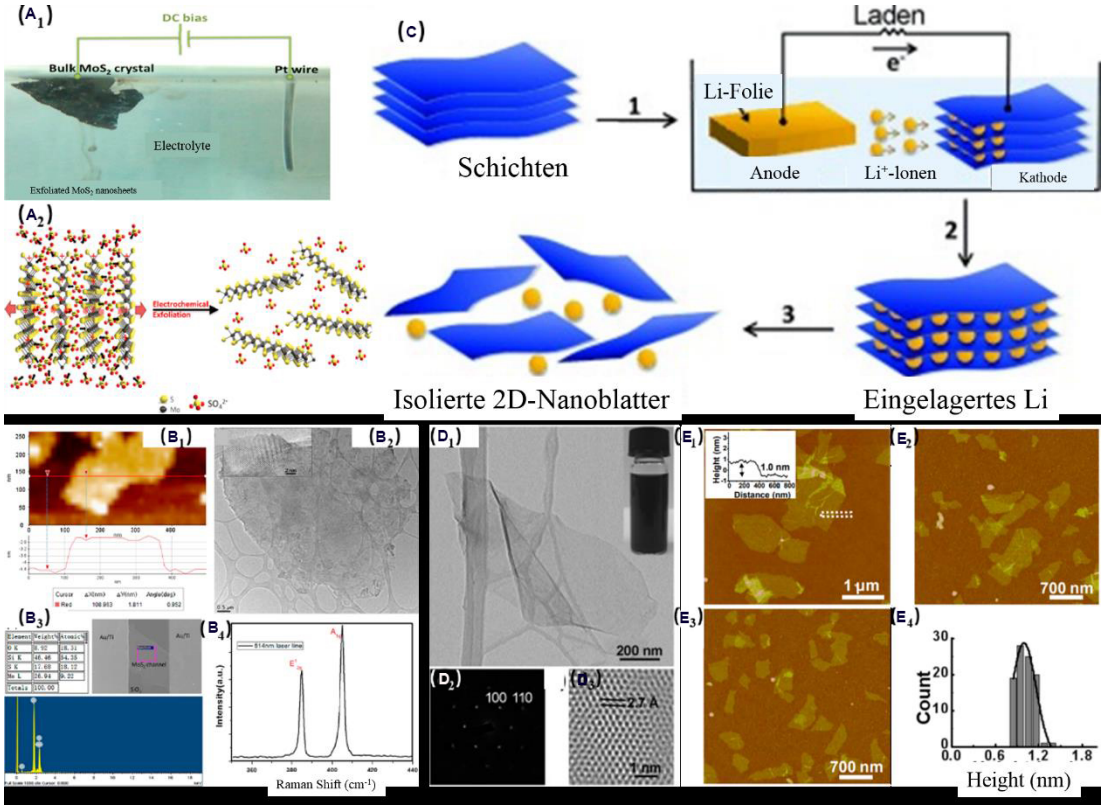

Figure 12. Stereogram (A_1) and schematic illustration of 2D MoS_2 electrochemical exfoliation experiment setup (A_2). AFM image (B_1), TEM image (inset: higher resolution TEM image) (B_2)[62], SEM-EDS (B_3) and Raman spectroscopy of 2D MoS_2 (B_4). Electrochemical lithiation process for 2D MoS_2 (C). TEM image (D_1), SAED pattern (D_2) and HRTEM image (D_3) of 2D MoS_2 and AFM images (E_{1-3}) and height distribution of 2D MoS_2 (E_4)[63].

Raman spectrum indicate that it has high crystallinity [Figure 12B3-4]. By this method, the obtained MoS_2 maintains its semiconducting properties, but its large-scale production remains difficult.

In order to improve the yield of 2D MoS_2, Zeng *et al.*[63] developed a method based on Li^+-assisted electrochemical exfoliation, which could promote the effective stripping of MoS_2. From the flow chart

shown in Figure 12C, it could be seen that lithium foil replaced the platinum electrode to become a new anode. When the current was released, Li^+ was inserted into the interlayer to reduce the Van der Waals forces between the layers of MoS_2. Subsequently, the MoS_2 after Li^+ intercalation was gradually stripped into highly dispersed 2D MoS_2 under ultrasonic action. Figure 12D1 shows the TEM image of 2D MoS_2, illustrating its high dispersion in the aqueous solution. The electron diffraction pattern in the flat region of the nanosheets [Figure 12D2] and the corresponding HRTEM image [Figure 12D3] show the hexagonal lattice structure with a lattice spacing of 2.7 Å distributed to the (100) crystal plane. The AFM measurement of 2D MoS_2 showed that its thickness was ~1.0 nm, thereby confirming the existence of 2D MoS_2. In addition, the slices of prepared 2D MoS_2 were detected by AFM, with 92% of them found to be monolayers [Figure 12E1-4]. The most obvious advantage of this method is that it cannot only control Li^+ insertion by controlling the working voltage, but that it also regulates the crystal phase of MoS_2 by adjusting the discharge process of the device.

Bottom-up methods

Vapor deposition

Both physical vapor deposition (PVD) and chemical vapor deposition (CVD) have been used to prepare 2D MoS_2. In PVD, the material source (solid or liquid) is vaporized into gaseous atoms or molecules or partially ionized into ions under vacuum conditions. Thin films are then deposited on the substrate surface through a low-pressure gas (or plasma) process, which is one of the main surface treatment technologies. Importantly, PVD is based on magnetron sputtering, meaning that extremely thin 2D films can be grown on very large areas of various substrate materials. Moreover, PVD has significant advantages in precisely defining the atomic scale, thickness control and interface cleanliness when processed in an ultra-high vacuum environment.

Nevertheless, the demands for controllable size, thickness, morphology and scalability have led to the dominant usage of CVD. CVD has been recognized as one of the preferred methods for preparing large-sized 2D MoS_2 with high crystal quality and uniform thickness. The main process is summarized as follows. The precursor containing Mo and S is decomposed into corresponding gaseous molecules under high temperature and specific atmospheric conditions, and then the reaction deposition is carried out on the substrate to generate 2D MoS_2. Among them, the most common is atmospheric pressure CVD (APCVD) with molybdenum trioxide (MoO_3) as the precursor. Of course, in addition to MoO_3, the molybdenum source mainly includes $MoCl_5$ and elemental Mo[64], while the sulfur source is mainly sulfur powder. Generally, MoO_3 and sulfur powder are placed in a single-zone tube furnace to effectively CVD grow MoS_2 on the substrate in an inert gas atmosphere [Figure 13A]. The reaction proceeds as a step-by-step vulcanization process described by three intermediate reactions[65]:

$$2MoO_3 + S \rightarrow 2MoO_2 + SO_2 \quad (1)$$

$$2MoO_2 + 5S \rightarrow 2MoOS_2 + SO_2 \quad (2)$$

$$2MoOS_2 + S \rightarrow 2MoS_2 + SO_2 \quad (3)$$

Perkgoz *et al.*[66] used APCVD to grow monolayer 2D MoS_2 and the deposition duration and temperature effect were systematically changed to better understand MoS_2 deposition and the influence of these parameters on the quality of the monolayer sheets. Figure 13B1-4 displays the TEM/HRTEM and SAED images of 2D MoS_2 to further understand its growth structure under better conditions. It can be seen that

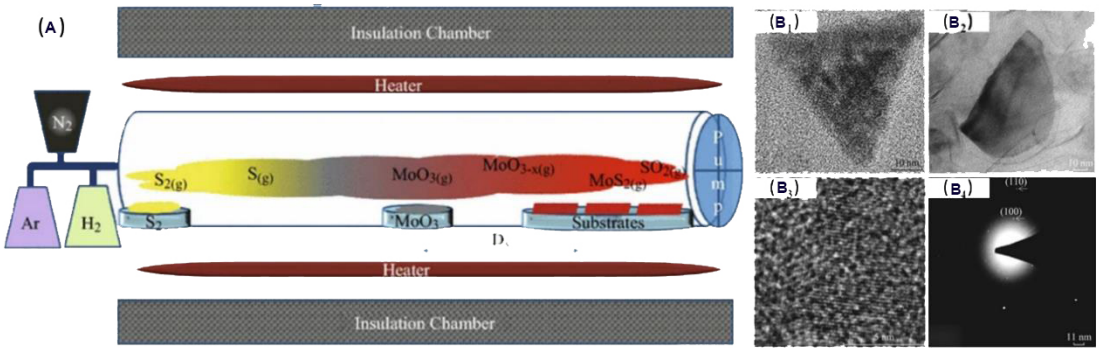

Figure 13. CVD system for deposition of 2D MoS_2 (A). TEM images (B_{1-2}), periodic atomic arrangement (B_3) and SAED pattern of 2D MoS_2 (B_4)[66]. CVD: Chemical vapor deposition.

2D MoS_2 with triangular and "chip" shapes were successfully grown, corresponding to the periodic atomic arrangement shown in Figure 13B3. The symmetry of the diffraction spots, as shown in Figure 13B4, indicates that the monolayer sheets were continuous single crystals with no rotational boundary, illustrating the high crystallinity of 2D MoS_2. Although the use of APCVD can achieve grain sizes of up to hundreds of microns of all-round growth, the process is seriously affected by many restrictions, such as overall thickness control, coverage uniformity and repeatability of operation. The variation in the characteristic morphology is related to the relative content of the precursor loaded into the reactor, leading to the consistency of the coverage and feature size remaining a challenge.

Metal-organic/organometallic chemical vapor deposition (MOCVD/OMCVD) is a new technology in which the gas molecules of organometallic compounds are sent to the reaction chamber with a carrier gas and undergo thermal decomposition reactions to form the compound. The first two letters, "MO" or "OM", refer to metal-organic or organometallic as the precursor for the growth of sheet. Chowdhury *et al.*[67] used $Mo(CO)_6$, a metal-organic compound, and $(C_2H_5)_2S$ as precursors, which were kept in bubblers in APs at 45 °C and room temperature, respectively [Figure 14A]. A large area of 2D MoS_2 was then deposited in a furnace at 850 °C for 1 min through a needle valve, which was uniformly covered and non-polluting on the whole substrate. The Raman spectrum in Figure 14B1 exhibits that there are two different peaks at ~386 and ~406 cm^{-1}, which are consistent with the vibrations of the Mo-S phonon mode E_{2g}^1 (in-plane) and A_{1g} (out-plane), respectively, thereby proving the existence of MoS_2. After vulcanization [Figure 14B2], most of the defect-induced peaks in the growth samples disappeared, indicating that the defect density decreased and the crystal quality improved.

Liu *et al.*[68] designed a bifunctional precursor, molybdenum dimethyldithiocarbamate (Mo-DMDTC), which is a metal-organic compound. The CVD diagram is displayed in Figure 14C. It is clear that Mo-DMDTC decomposes at elevated temperatures, providing a Mo source for the CVD growth of MoS_2. Importantly, the presence of organic compounds reduces the free energy of MoS_2 nucleation on the substrate, namely, organic promoters, which also greatly promote the growth of MoS_2 [Figure 14D1]. The UV-vis spectra [Figure 14D2] show that when the molar ratio of DMDTC and Mo^{5+} reached five, the absorbance was close to saturation, indicating that the coordination number of Mo was close to five. A large area of triangular 2D MoS_2 with a length of 20-30 μm, was obtained on a sapphire substrate based on CVD, as shown in Figure 14D3. The thickness scan analysis of AFM suggested that the thickness of triangular MoS_2 was ~0.65 nm, corresponding to monolayer MoS_2 [Figure 14D4].

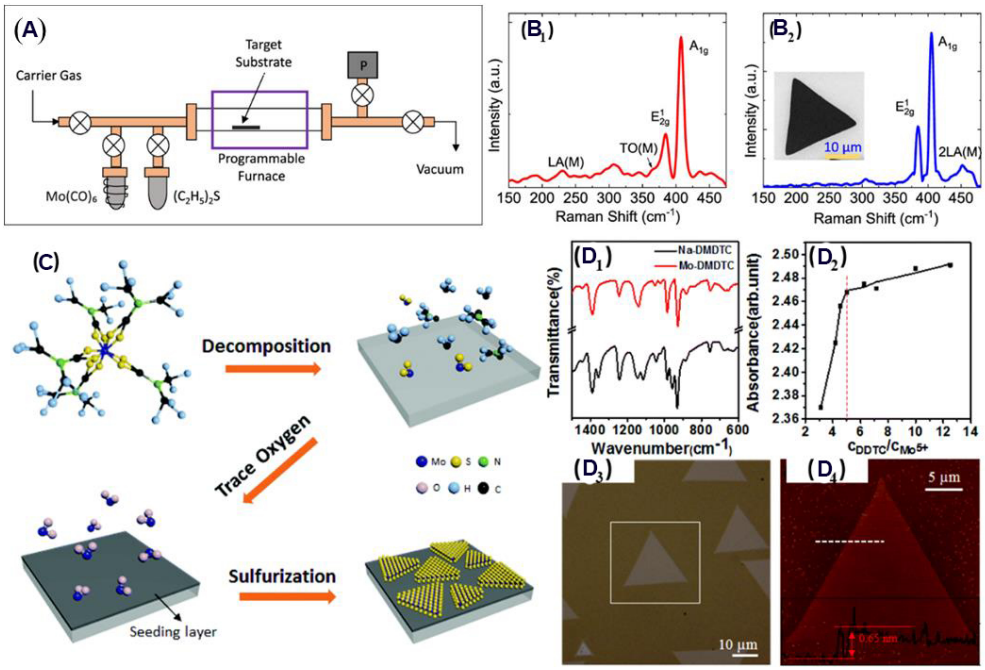

Figure 14. Schematic of MOCVD growth system (A)[67]. Raman spectrum of MoS_2 films before (B_1) and after (B_2) sulfurization at 850 °C for 30 min (inset: SEM image of a triangular MoS_2 domain following sulfurization). Schematic of 2D MoS_2 synthesis (C). FTIR spectra of Na-DMDTC and Mo-DMDTC (D_1). UV-vis absorbance (at 210 nm) of the mixture of Na-DMDTC and $MoCl_5$ with varied molar ratios (d_2). Optical image of 2D MoS_2 (D_3). AFM image of 2D MoS_2 marked with a square box in (D_4)[68].

In order to prepare large-sized and uniform 2D MoS_2 with excellent electrical properties, researchers have subsequently proposed the thermal decomposition of precursors containing both molybdenum and sulfur atoms. Compared with MoO_3 and $MoCl_5$, the method based on the pyrolysis of $(NH_4)_2MoS_4$ to grow 2D MoS_2 has the advantages of a single precursor source and large growth window and therefore the potential for large-scale production. Fei *et al.*[69] in-situ observed the thermal decomposition of $(NH_4)_2MoS_4$ and subsequent 2D MoS_2 crystallization behavior by TEM [Figure 15A]. The pattern evolution with increasing temperature, as exhibited in Figure 15B1-4, was clearly observed by SAED. From room temperature (25 °C) to 400 °C, 780 °C and then 900 °C, the pattern displays no diffraction ring, a fuzzy diffraction ring, a sharper bright diffraction ring and then a discrete diffraction ring, respectively. In summary, the crystallization of MoS_2 occurs at 400 °C-900 °C in the vacuum, the crystal size of MoS_2 increases rapidly after 800 °C and MoS_2 finally decomposes at high temperature. The reaction equation of $(NH_4)_2MoS_4$ pyrolysis to MoS_2 in a N_2 environment is shown as follows:

$$(NH_4)_2MoS_4 \rightarrow 2NH_3 + H_2S + MoS_3\,(120\ ^\circ C\text{-}360\ ^\circ C) \quad (4)$$

$$MoS_3 \rightarrow MoS_2 + S\ (>800\ ^\circ C) \quad (5)$$

The average grain size of MoS_2 increases with increasing temperature (820-850 °C), i.e., it is 3.2 nm at 820 °C, 6.5 nm at 840°C and 18.5 nm at 850 °C [Figure 15D1]. The same test result can also be observed in the in-situ TEM images of Figure 15C1-4. Figure 15D2 exhibits the in-situ Raman spectra of the fresh chips, including the $(NH_4)_2MoS_4$ precursor and the grown MoS_2 (annealed at 850 °C for 30 min). Notice that the peak intensity of E^1_{2g} is over 50% of the A_{2g} peak, suggesting the horizontal growth of MoS_2. The distance between the two Raman peaks is ~25.5 cm^{-1}, corresponding to four to five layers of MoS_2. Compared with

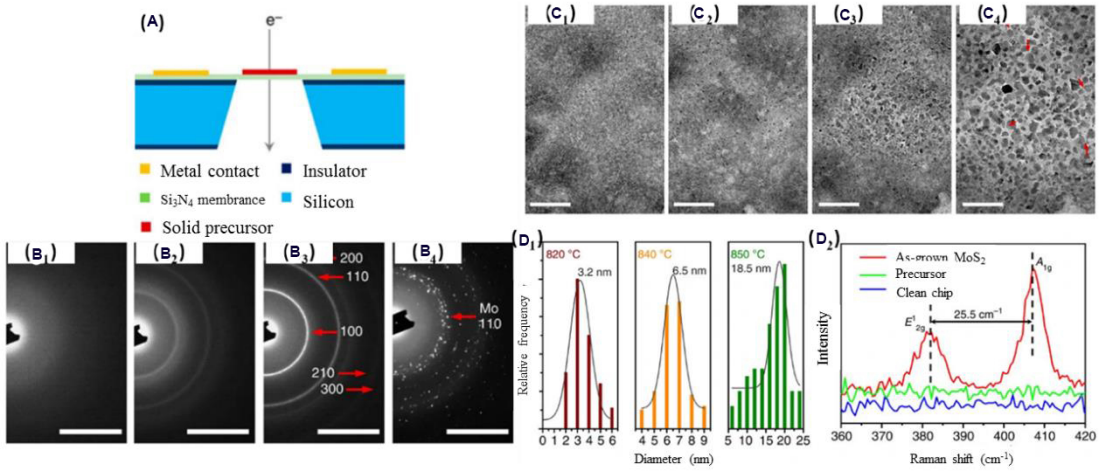

Figure 15. Schematic side view of experimental setup of in-situ TEM heating stage (A). Evolution of SAED patterns across a wide temperature range (B_{1-4}): 25 °C (B_1); 400 °C (B_2); 780 °C (B_3); 900 °C (B_4). TEM images showing the size of 2D MoS_2 increasing with increasing temperatures (C_{1-4}): 800 °C (C_1); 820 °C (C_2); 840 °C (C_3); 850 °C (C_4). Statistical distribution of 2D MoS_2 size as a function of heating temperature from c_{1-4} (D_1). Raman spectra of silicone chip, $(NH_4)_2MoS_4$ precursor and as-grown MoS_2 (D_2)[69].

other preparation methods, the vapor deposition method can be used to prepare single- or few-layer MoS_2 with a large diameter, and the synthesized 2D MoS_2 has the advantage of high crystallinity. However, the operation process of this method is extremely complex and the energy consumption is very high, so it is still unable to realize the mass production of 2D MoS_2.

Hydrothermal/solvothermal method

Hydrothermal/solvothermal syntheses are typical bottom-up methods that are widely used in the synthesis of 2D MoS_2, owing to their simplicity, high efficiency and strong adaptability. Generally, the Mo source (e.g., MoO_3, ammonium molybdate or sodium molybdate) and S source (e.g., sulfur powder, KSCN or thiourea) are dissolved in an aqueous solution/organic solvent at a certain ratio. The solution is then transferred to a sealed reactor and kept at ~200 °C for a certain period (several to more than ten hours), with 2D MoS_2 then obtained after the reaction. According to the different precursor or preparation conditions (temperature, solution pH, and so on), a variety of nanostructured MoS_2 can be easily obtained, including granular, flakes, flower-like microspheres and so on. 2D MoS_2 can be obtained by the hydrothermal treatment of ammonium tetrathiomolybdate at 350 °C in different solution pH values and the SEM images are shown in Figure 16A1-3[70]. The samples prepared at pH 4.5 are composed of aggregates that are irregularly shaped and interconnected [Figure 16A1], while the samples prepared at pH 7 are composed of particles with different shapes, rather than aggregates [Figure 16A2]. In contrast, the samples prepared at pH 9.5 are flower-like, consisting of petals with a thickness of 10 nm and lengths of 100-200 nm [Figure 16A3]. These petals aggregate to form microspheres of 300-400 nm, with an increase in pH from 4.5 to 9.5, leading to the aggregation of thin nanosheets into flower-like MoS_2.

Furthermore, 2D MoS_2 can also be grown on carbon felt using phosphomolybdic acid and thiourea at different temperatures, as shown by the macroscopic SEM images in Figure 16B1-3 and the corresponding microscopic SEM images in Figure 16B4-6[71]. The structure of MoS_2-180 °C is a well-assembled multi-faceted nanoflower with a diameter of 200-300 nm, which is composed of crosslinked nanosheets. As the temperature rises to 240 °C, 2D MoS_2 aggregates into larger particles and forms clusters on the surface of the carbon fibers. The three samples all have a 2D layered structure and the stacking structure becomes more

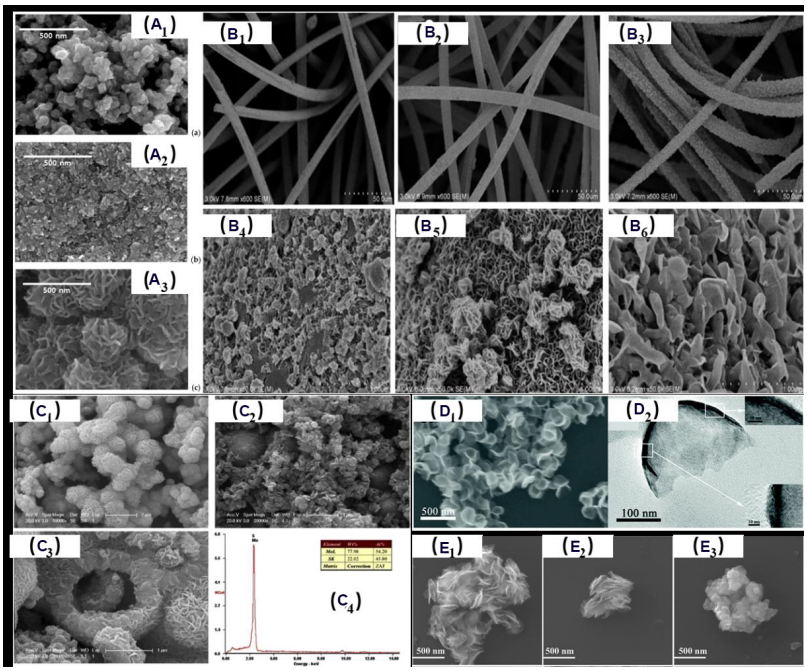

Figure 16. SEM images (A_{1-3})[70] of 2D MoS_2 prepared at pH 4.5 (A_1), pH 7.0 (A_2) and pH 9.5 (A_3). SEM images (B_{1-6}) of MoS_2-160 °C ($B_{1,4}$), MoS_2-180 °C ($B_{2,5}$) and MoS_2-240 °C ($B_{3,6}$) before inoculation[71]. SEM (C_{1-3}) and EDS (C_4) spectrum of as-prepared MoS_2[72]: flowerlike (C_1); nanosheet (C_2); hollow MoS_2 (C_3). SEM image of MoS_2 RNPs (D_1). TEM image of an MoS_2 RNP (the inset images reveal that the edge thickness was ~10 nm) (D_2)[73]. SEM images (E_{1-3}) of PW-MoS_2 (E_1), MWP-MoS_2 (E_2) and PP-MoS_2 (E_3)[74].

obvious with increasing synthesis temperature. In addition, Wu *et al.*[72] used CTAB as a surfactant to assist in the preparation of 2D MoS_2 with various shapes under different growth conditions, including hollow, nanosheets and flower-like [Figure 16C1-3]. Figure 16C4 shows that the nanomaterials are composed of Mo and S with a stoichiometric ratio (Mo:S) of 1:2, with no other elements detected by EDS, indicating pure MoS_2.

Interestingly, 2D MoS_2 with a special shape was obtained by the hydrothermal treatment of sodium molybdate dihydrate and thioacetamide at 200 °C for 36 h, as indicated by the SEM and TEM measurements in Figure 16D1-2, which reveal the morphology of the product[73]. Finally, 2D MoS_2 with a diameter of ~200 nm and an edge thickness of ~10 nm is observed, which is similar to morphology of radar. Furthermore, the solvothermal method is also a simple and efficient method to synthesize 2D MoS_2. Chen *et al.*[74] synthesized ultrathin 2D MoS_2 with ammonium molybdate tetrahydrate and thiourea assisted by polyethylene glycol (PEG). 2D MoS_2 prepared with PEG and pure water, as solvents, was labeled as MWP-MoS_2, pure water was PW-MoS_2 and pure PEG was PP-MoS_2. The prepared PW-MoS_2 was clustered and composed of densely stacked nanosheets. MWP-MoS_2 showed a highly folded surface and layered structure. For PP-MoS_2, the agglomeration of nanoparticles was observed and was obviously composed of randomly oriented layers rather than regular stacked layers [Figure 16E1-3].

3D MoS_2-based materials

Despite a large number of approaches for the synthesis of 3D MoS_2-based materials having been developed, a clear classification has not yet been established. Here, the synthetic strategies for 3D MoS_2-based materials are briefly outlined and divided into three types, namely, template-based, self-assembly and sol-gel methods.

Template-based method

2D MoS_2 can be anchored on the surfaces of some templates (including sponge, aerogel and carbon matrix) that possess a 3D architecture via the hydrothermal method, CVD or impregnation method[75,76]. Benefitting from the facile preparation process, the structural and physical properties of 3D MoS_2-based materials can be easily modified by changing the template. Zhu *et al.*[77] prepared a 3D-MoS_2 sponge by anchoring MoS_2 nanosheets and graphene oxide (GO) on the skeleton of a sandwich-structured sponge via a simple two-step impregnation method. A blank melamine sponge was dipped into MoS_2 and GO alcohol solutions in sequence to obtain a 3D sponge@MoS_2@GO after a simple heat treatment at 200 °C in an oven for 6 h [Figure 17A]. This material could adsorb organic molecules and provide multidimensional electron transport pathways, as well as exhibit excellent performance in the degradation of aromatic organics. A 3D porous MoS_2/chitosan aerogel with excellent mechanical strength and stability was constructed by anchoring MoS_2 to the surface of the chitosan aerogel[78]. Benefitting from the superior photocatalytic performance and porous networks, which promote the mass transfer and shorten the diffusion pathway of the substances, the MoS_2/chitosan aerogel can effectively recover gold from a thiosulfate solution via the direct in-situ reduction of Au(I) to Au^0 under sunlight.

In order to improve the application performance of MoS_2 nanosheets in lithium-ion battery anodes and water electrolysis, 2D MoS_2 can be anchored on the skeleton of a conductive 3D matrix, such as 3D porous carbon aerogels (CAs)[79], carbonized cellulose aerogels[80], 3D nickel and CAs[81], graphene foam[82] and carbon cloth[83], which avoids the aggregation and restacking of 2D MoS_2 and ensures the fast transport of both electrons and ions during the electrochemical process. A CA was synthesized by Zhang *et al.*[79] through the combination of a sol-gel process and high-temperature carbonization and 2D MoS_2 was subsequently decorated on its skeleton via a solvothermal treatment to obtain a MoS_2/CA aerogel [Figure 17B-E]. The resulting composite was carbonized at 900 °C to obtain a lightweight MoS_2/cellulose nanofiber (CNF) aerogel with a hierarchical structure [Figure 17F-H][84]. A novel 2D spatial confinement strategy to in-situ fabricate 2D MoS_2 anchored on 3D porous carbon nanosheet networks was demonstrated by Zhou *et al.*[85], in which highly crystalline MoS_2 nanosheets with five or fewer layers very homogeneously and tightly lie on the surface of carbon nanosheet walls (with thickness a ≥ 3 nm). The novel 3D architecture composite exhibited an outstanding long-life cycling capability at high rates, i.e., a specific capacity as large as 709 mAh g^{-1} was delivered at 2 A g^{-1} and maintained at ~95.2% even after 520 deep charge/discharge cycles.

Self-assembly

3D MoS_2-based materials have been frequently fabricated with the assistance of GO, owing to its self-assembly feature during the reduction process. When a MoS_2 suspension is mixed with a GO suspension, 2D MoS_2 is prone to deposit on the surface of GO. With a decrease in the oxygen-containing group content on GO during thermal or chemical reduction, the hydrophobicity and internal π-π interactions between GO nanosheets are enhanced, resulting in the aggregation and formation of a MoS_2-graphene hydrogel[86]. Finally, MoS_2-graphene aerogels can be obtained after freeze-drying. 3D MoS_2/graphene aerogels are mainly applied in supercapacitors and lithium/sodium-ion batteries because the constructed 3D architecture facilitates electrolyte ion transport and improves the electrochemical performance through electric double-layer and faradaic pseudo-capacitance[87-89].

3D hybrid aerogels of MoS_2 nanosheet/nitrogen-doped graphene (3D MoS_2/N-GAs) with a large surface area and high electrical conductivity were fabricated by Liu *et al.*[90] using urea as a reductant [Figure 18A]. A 3D free-standing cylinder was obtained after the reaction, in which the MoS_2 nanosheets were uniformly anchored onto graphene sheets with interconnected pores ranging from several nanometers to several

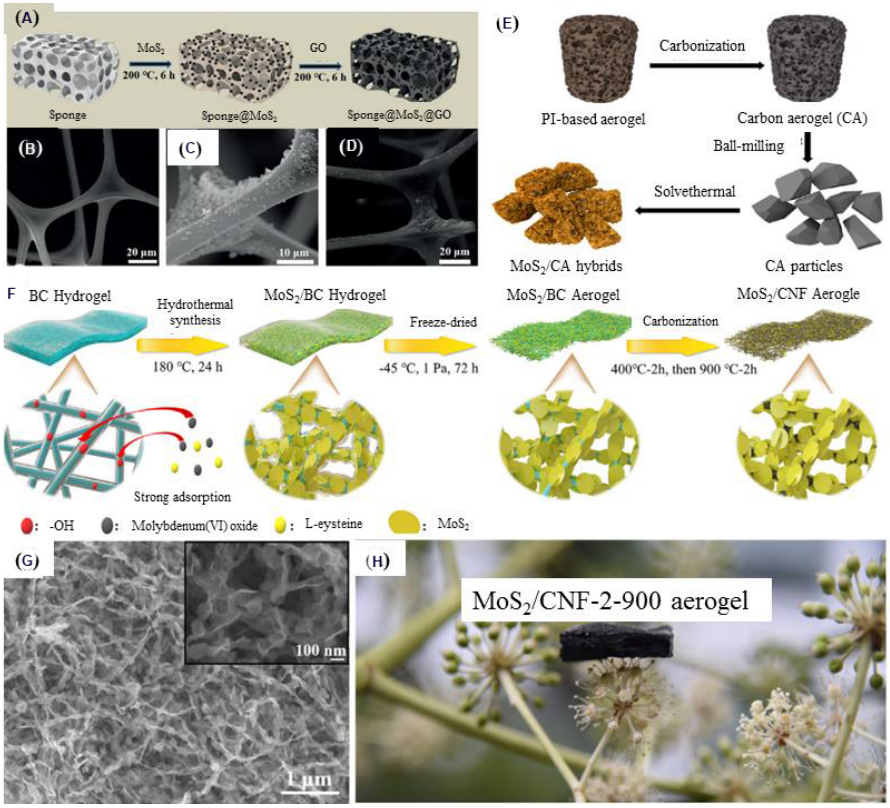

Figure 17. Synthetic pathway of sponge@MoS_2@GO (A) and SEM images of sponge (B), sponge@MoS_2 (C) and sponge@MoS_2@GO (D)[77]. Schematic of MoS_2/CA hybrid preparation (E)[79]. Schematic of MoS_2/CNF aerogel fabrication (F) and SEM image (G) and physical appearance (H) of MoS_2/CNF-2-900 aerogel[84].

micrometers [Figure 18B-D]. When used as a supercapacitor electrode material, this hybrid aerogel exhibited an excellent specific capacitance of 532 $F \cdot g^{-1}$ at a current density of 1 $A \cdot g^{-1}$ and superior cycling stability of 93.6% capacitance retention after 10000 cycles at 10 $A \cdot g^{-1}$, which was significantly higher than those of 2D MoS_2 and nitrogen-doped graphene aerogels alone.

To reduce the reliance on polymeric binders, conductive additives and metallic current collectors during the electrode preparation process, as well as to assess the true performance of lithium-ion battery anodes, a MoS_2-anchored graphene aerogel paper (MGAP) was synthesized by Lee *et al.*[91] via a self-assembly and compression process [Figure 18E]. The fabricated MGAP, with a density of 0.47 g cm^{-3} and a surface area of 5.5 $m^2 g^{-1}$, was able to undergo 180° bending [Figure 18F] and MoS_2 was successfully incorporated into the aerogel paper [Figure 18G]. Another method of one-pot freeze-drying self-assembly combined with in-situ thermal decomposition-reduction for 3D MoS_2/graphene aerogel preparation was proposed by Wang et al.[92], with significant potential for scale-up. A precursor aerogel was first constructed via the self-assembly of $(NH_4)_6Mo_7O_{24}$ and CH_4N_2S-loaded GO nanosheets. Upon the subsequent in-situ thermal decomposition-reduction treatment process, $(NH_4)_6Mo_7O_{24}$ and CH_4N_2S were decomposed to MoO_3/NH_3 and NH_3/H_2S, respectively [Figure 18H]. MoO_3 was subsequently in-situ reduced to MoS_2 by reacting with H_2S and GO was reduced to graphene nanosheets, giving rise to the final MoS_2/GS aerogels.

Sol-gel method

3D MoS_2-based materials can also be fabricated via a sol-gel process and subsequent drying to remove the solvent. During the typical process of gelation, the sol-gel transition of MoS_2 nanosheets creates a 3D

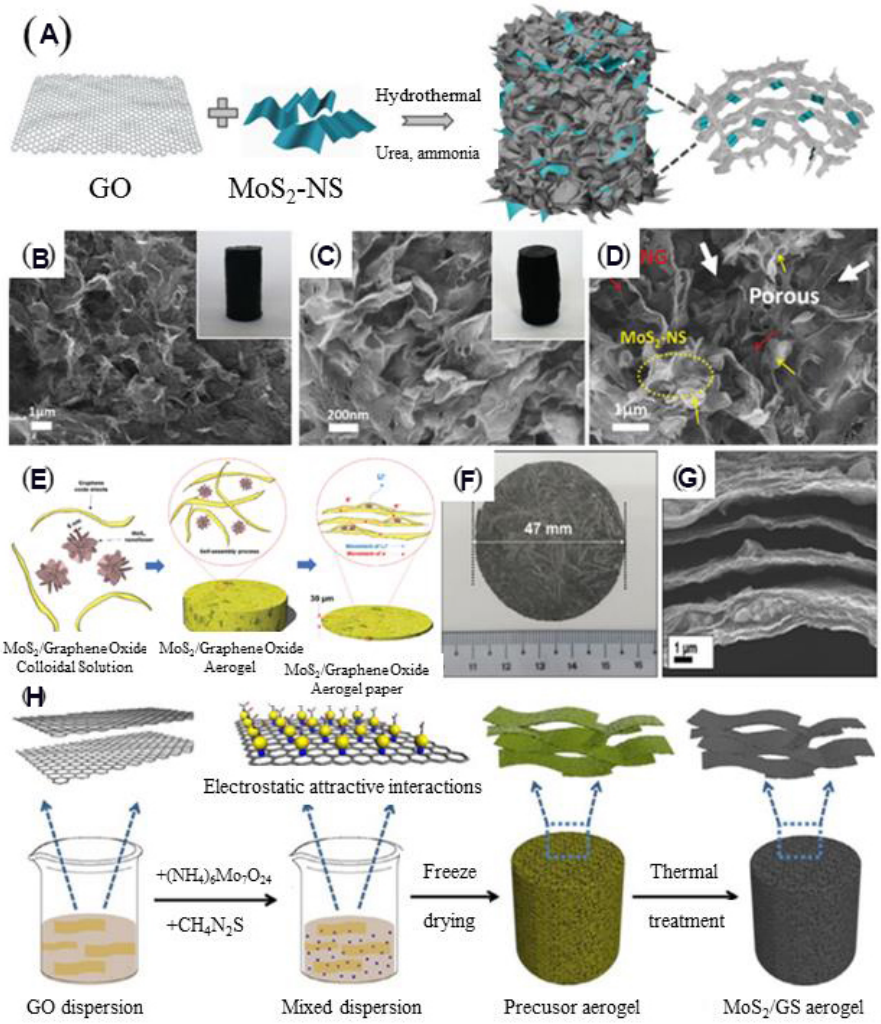

Figure 18. Schematic of the synthesis process of 3D MoS_2/N-GA porous aerogel hybrids (A). SEM images of N-doped graphene aerogel (B) and 3D MoS_2/N-GAs (C-D)[90]. Schematic of MGAP fabrication process (E) and photographic and SEM images of MGAP (F-G)[91]. Schematic of the fabrication process of MoS_2/GS hybrid aerogels (H)[92]. MGAP: MoS_2-anchored graphene aerogel paper.

network by polymeric binders through physical or chemical crosslinking[93,94]. A method of vacancy-driven gelation to obtain chemically crosslinked hydrogels from defect-rich MoS_2 nanoassemblies and polymeric binder was reported by Jaiswal *et al.*[95]. The defects of MoS_2 nanoassemblies acted as active centers for vacancy-driven gelation with a thiol-activated terminal, such as four-arm poly(ethylene glycol)-thiol(PEG-SH) via chemisorption, forming an elastomeric and robust gel [Figure 19A]. The MoS_2 nanoassemblies were completely encapsulated by PEG-SH, endowing a remarkable mechanical resilience for the PEG-SH/2% MoS_2 hydrogel that could be stretched, bended and twisted easily [Figure 19B]. Furthermore, the hydrogel had an interconnected porous network with a pore size of ~10 μm [Figure 19C and D].

The lack of connecting/bonding sites in the part of functional groups greatly limits the construction of high-quality MoS_2 aerogels. The functionalization of 2D MoS_2 was achieved by Wang *et al.*[96] via the self-polymerization of dopamine monomers, rendering MoS_2 nanosheets rich in functional groups, such as catechol, amine and imine. A 3D MoS_2 aerogel could then be facilely constructed under the crosslink of the functionalized MoS_2 nanosheets and chitosan [Figure 19E]. The resulting MoS_2 aerogel could stand on a

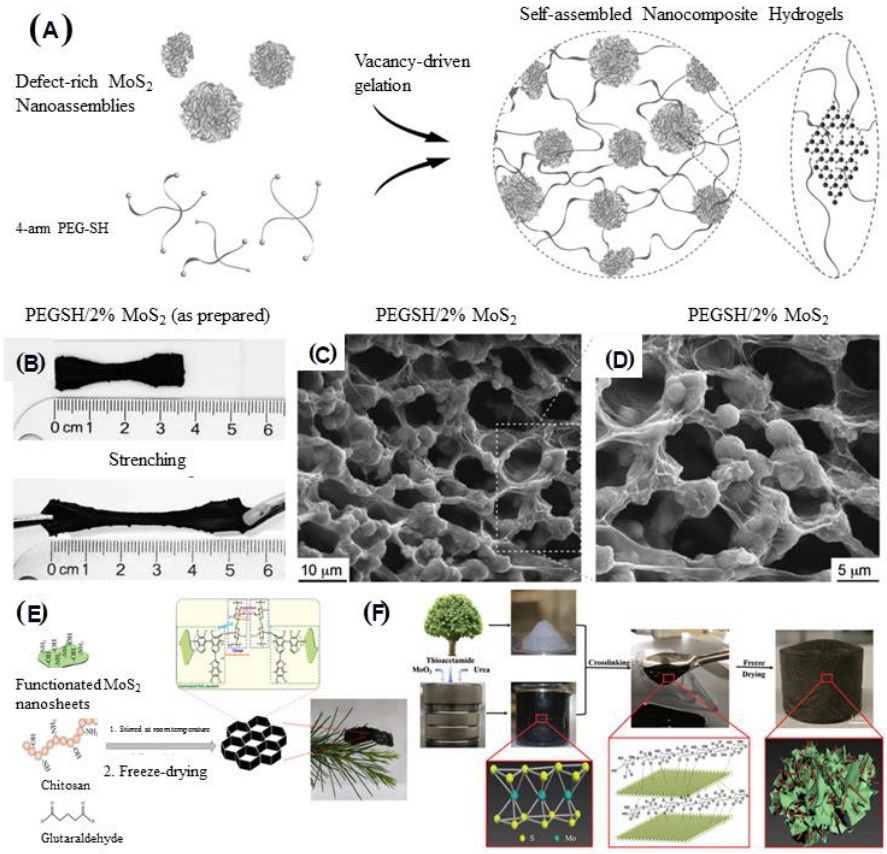

Figure 19. Schematic of PEG-SH/MoS_2 hydrogel synthesis mechanism (A) and photographs (B) and SEM images of PEG-SH/MoS_2 hydrogel (C, D)[95]. Schematic of preparation strategy of 3D MoS_2 aerogel (E)[96]. Schematic of the growth process of CNF/MoS_2 aerogel (F)[97]. SEM: Scanning electron microscope; PEG-SH: poly(ethylene glycol)-thiol.

flexible cedar leaf without changing its original shape, revealing the high porosity and ultralight properties of 3D MoS_2. Furthermore, Mo^{4+} was presented in metallic MoS_2, which links with carboxyl (-COOH) and hydroxyl (-OH) groups in the cellulose chains to form crosslinked metal-carboxylate complexes. These complexes allowed the 2D MoS_2 to effectively encapsulate theCNF at the nanoscale, based on which Yang *et al.*[97] synthesized an ultralight, highly porous CNF/MoS_2 aerogel with good mechanical strength via a combined sol-gel and freeze-drying process [Figure 19F].

Due to the encapsulation of 2D MoS_2 by polymeric binders, the catalytic activity and conductivity of 3D MoS_2 prepared by the sol-gel method may be weakened, thereby restricting its application in the fields of supercapacitors, lithium-/sodium-ion batteries and electrochemical hydrogen production. Therefore, these 3D MoS_2 aerogels are primarily applied in the field of solar desalination, fire retardants and microwave adsorption[98] with the utilization of their physical properties.

MODIFICATION

Modification for surface defects

The crystal anisotropy of MoS_2 makes it exhibit discrepant properties between "surface" and "edge" sites. In particular, the "edge" sites show more active chemical reactivity, such as adsorption[99], photocatalysis[100] and electrochemistry[101], which is beneficial for their applications in relevant fields. Based on this characteristic of the MoS_2 structure, executing defect engineering on "surface" sites to induce more neonatal "edge" sites

represents an effective method for the optimization of chemical performance. In the past few decades, numerous studies regarding defect-modified MoS_2 have been reported, thereby illustrating the importance of defect engineering in current MoS_2 research. According to the dimensionality, the defect types in MoS_2 can be mainly classified into two categories: (1) point-like defects and (2) plane-like defects.

Point-like defects

Point-like defects in MoS_2 include anionic, cationic and hybrid vacancies, which are generated from the movement of lattice atoms from their original sites, i.e., internal defects. The existence of point-like defects destroys the crystal lattice of MoS_2, leading to the regulation of its chemical properties and electrical configuration[102]. So far, numerous studies have attempted to produce point-like defects in MoS_2.

Point-like defects in MoS_2 can be induced by the irradiation of particles, i.e., irradiation-induced defects. Normally, particle irradiation is produced from special equipment, such as a tandem accelerator. As illustrated in Figure 20A, when particles with high energy are shot at the MoS_2 surface, the lattice atoms passively release from their original sites to leave point-like defects in the crystal structure[103]. Importantly, the density of the point-like defects is accurately regulated by controlling the irradiation strength. As shown from the high angle annular dark-field (HAADF) images in Figure 20B, with increasing Ca^+ irradiation strength, it can be seen that the quantity of point-like defects (the black holes in the images) gradually increases[104]. Various sources of radiation, including heavy ions, electrons, protons, X-rays, gamma rays, ultraviolet light and infrared irradiation, have been carried out with this technique[105].

Heavy ions with high energies are generally accelerated by particle accelerators. Mishra *et al.*[106] used a Ga flux beam under ultrahigh vacuum conditions to irradiate MoS_2. As a result, the Raman signals and XPS spectra of the Mo-3d orbital exhibited an obvious shift, revealing that the original atoms in MoS_2 were replaced by Ga atoms. Furthermore, other heavy metals, including uranium[107], xenon[108], bismuth[109] and manganese[110], have also been adapted to irradiate MoS_2 and successfully induce point-like defects on its surface. In addition, similar procedures to induce point-like defects have been carried out by using other irradiation particles. In conclusion, although the generation of point-like defects in MoS_2 by particle irradiation is a mature technique, it requires specialistic equipment, which limits its popularization.

In addition, the hydrothermal method is another technique to prepare MoS_2 with point-like defects. During the synthetic procedure, the precursors of Mo and S are firstly dissolved in water and transferred into a closed container. Subsequently, MoS_2 crystals form and gradually grow under an environment of high temperature and pressure. It is noteworthy that the microstructure of synthesized MoS_2 can be regulated by adding different molar ratios of the Mo and S precursors. Normally, when the molar ratio of Mo and S atoms breaks the balance of 1:2, point-like defects will form in the MoS_2 structure. MoS_2 samples with different concentrations of point-like defects were synthesized via a hydrothermal method by Chen *et al.*[111] and the majorization of the piezoelectric response for gold recovery was realized. Furthermore, according to the report of Jayabal *et al.*[112], 1T-MoS_2 samples with point-like defects were prepared using a hydrothermal strategy and exhibited excellent performance in the hydrogen evolution reaction. As a consequence, point-like defects produced by the hydrothermal technique were executed by only using a Teflon-lined stainless steel autoclave, making it a facile method for wide research applications.

Plane-like defects

Compared to the formation of point-like defects, the generation of plane-like defects in MoS_2 requires more energy from the environment to destroy the crystal structure, thus to form a large area of vacancies. As a common method, thermal annealing is an effective method of inducing large-scale edges through the

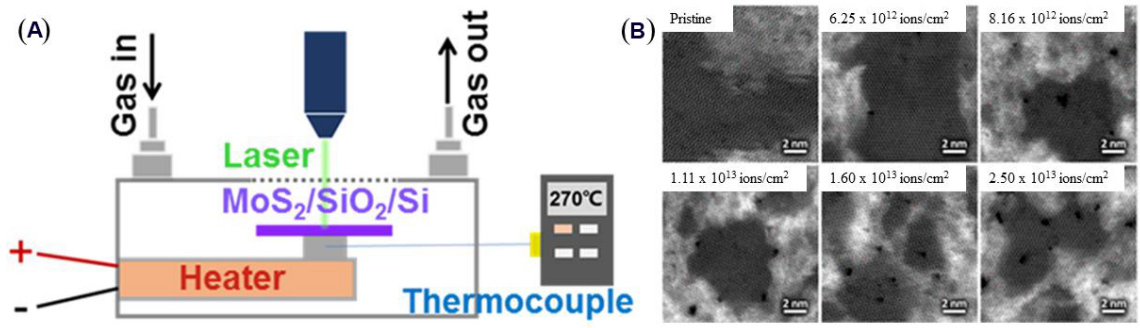

Figure 20. Schematic of inducing defects in MoS_2 by irradiation (A)[103].HAADF images of MoS_2 after Ga^+ irradiation under various strengths (B)[104].

etching of the MoS_2 crystal. By simply undergoing heating, plane-like defects could be induced in MoS_2. Importantly, the degree of defects can be regulated through the selection of reaction atmosphere and temperature. Jia *et al.*[113] studied the formation rule and mechanism of edge defects in MoS_2 through thermal treatment. As shown from the AFM images in Figure 21, MoS_2 displays different areas of plane-like defects after thermal treatments under various conditions. A larger etched area is induced at higher temperature and oxygen content in order to achieve good control of plane-like defects in MoS_2. Meanwhile, the shape of the defects oriented to equilateral triangular pits, which was ascribed to the trigonal prismatic 2H phase of MoS_2[114]. Relevant research has been reported for further understanding the technique mechanism and a similar conclusion was reached[115,116]. Using this thermal treatment method, numerous properties of MoS_2 have been improved and widely applied in desalination[117] and adsorption[99].

Heteroatom doping

Heteroatom doping is an effective method to tune both the chemical and physical properties of MoS_2. Dopants in MoS_2 can substitute at either the Mo or S site. Furthermore, they can exist at the surface or as adatoms on the basal plane or an edge on an MoS_2 sheet. Dopants occur in some high symmetry sites, for example, atop S, atop Mo and at the center of a hexagonal hollow[2].

Doping atoms affect the local structure, lattice parameters and even the overall crystal structure of MoS_2. For instance, the intercalation of Li atom changes the crystal structure type from 2H to 1T, and the substitution of Mo by Nb changes it from 3R to 2H. Furthermore, the crystal and morphology are influenced by dopants through kinetic or thermodynamic effects. Many synthetic processes occur in non-equilibrium conditions, so theoretical studies are complicated.

Dopants can generally be considered in the context of the following factors. One important factor is whether the ionic radius of the doping atoms is similar to the radii of the Mo and S atoms. Whether the doping atoms possess similar bond lengths with Mo or S compared with the corresponding bond length in MoS_2 is another vital point. Doping atoms are chosen as a 4+ oxidation state to fit the Mo site and a 2- oxidation state to fit the S site. With regard to intercalated dopants, the atoms are neutral. In synthetic conditions, the doping location can be controlled by adjusting the chemical potentials of Mo, S and the dopant; for instance, an S-rich environment will benefit the substitution of Mo. Possible dopants include transition metals and chalcogens[118-127].

Since 2013, many researches have attempted to dope heteroatoms into MoS_2 and doping methods based on the following three strategies have been established[128]:

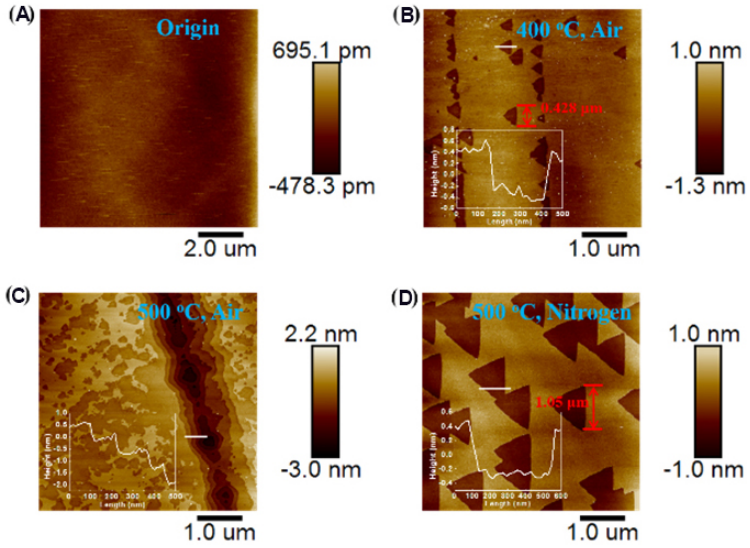

Figure 21. AFM images of MoS_2 after thermal treatments under different conditions [Origin MoS_2 (A); 400℃ for 2 h in air (B); 500℃ for 2h in air (C); 500℃ for 3h in N_2 (B)][113].

(i) Charge transfer doping, where the type and concentration of photoelectrons can be regulated by surface charge transfer that is realized by depositing and adsorbing small molecules and polymers on the surface of MoS_2;

(ii) Substitutional doping, where dopants are introduced to replace Mo or S atoms to regulate the band structure and transport characteristics of MoS_2 by forming in-plane covalent bonds during or after growth, and the material properties are further enriched by introducing heteroatoms;

(iii) Intercalation doping, where the structure and electrical transport characteristics can be controlled by the interlayer insertion of atoms, molecules or ions.

Charge transfer doping

Charge transfer doping is realized by either physical or chemical interactions between dopants and the supporting material, and the dopants originate from gas (O_2 and NO_2), metal or compound molecules. Dopants can attach to MoS_2 via adsorption, deposition and spin and dip coating. The doping degree can be determined by Raman spectroscopy, the PL peak position and intensity charge, the XPS peak position shift, the change in source-drain current-gate voltage response in electrical measurements, Hall measurements and so on[129]. The activity of the charge transfer direction is governed by the difference at the Fermi level (E_F). The main experimental methods to characterize the doping effect include determining the type and which created by the dopants and supporting materials [Figure 22A][121]. If the E_F of the dopants is lower than that of the supporting materials, electrons will be transferred from the supporting materials to the dopants, i.e., p-type doping. In contrast, n-type doping is based on the electron transfer from dopants to supporting materials. Generally speaking, the interaction regarding charge transfer happens on the interface of any adjacent media, like particle ions, surface atoms, molecules and supporting materials[23,130-132]. The advantage of charge transfer doping is enhancing the electronic behavior of semiconductors whilst avoiding lattice distortion and high mobility transport.

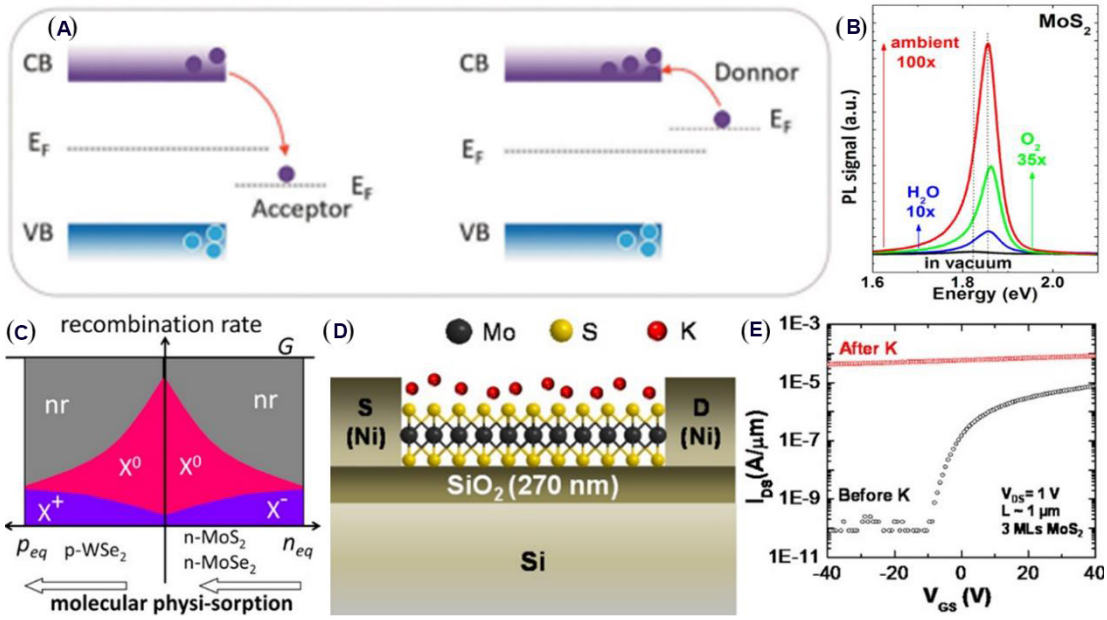

Figure 22. Behavior of charge transfer doping (A)[121]. Modulation of PL property of MoS_2 via exposure to various gas atmospheres and the change in exciton and non-radiation recombination (B and C)[137]. Electrical characteristics of K-doped MoS_2 (D-E)[134].

The main purposes of charge transfer doping are changing the work function of the material and reducing the Schottky barrier between the material and electrode with an improvement in device performance[133]. It also regulates the type and concentration of carriers in the channel to obtain high-performance devices with electrons (n-type) or holes (p-type) as the main carriers or to construct space charge regions (p-n junction) to provide basic structural elements[134]. Finally, charge transfer doping can be used to turn the field-effect transistor by constructing a steep in-plane tunneling junction with high heterogeneity.

Gas molecules are often adsorbed on the surface of MoS_2 and then turn the optical and electronic behavior of the supporting materials[135]. This characterization is applied in gas sensing, in which semiconductor materials are employed as the sensing channel[136]. The simplest method of gas-phase doping is to directly expose MoS_2 to a target atmosphere. The usual interaction is physical adsorption via weak van der Waals interactions, where desorption is possible. During thermal annealing in a vacuum, the exposure effect will be strengthened. This process can clean unnecessary contaminants and increase the concentration of S vacancies, which promote the adsorption of gas molecules.

Tongay *et al.*[137] found that after exposing MoS_2 to various atmospheres, such as O_2, H_2O, ambient and inert gases, the PL intensity in n-type MoS_2 was obviously enhanced because of the depletion of electrons and the suppression of non-radiative recombination [Figure 22B and C]. The PL intensity is much higher than that under a vacuum and increases by 10×, 35× and 100× after exposure to H_2O, O_2 and air, respectively, and the peak shifts from 1.84 to 1.88 eV. However, the PL intensity and peak position remain unchanged when the air is changed to Ar and N_2. When the inert gas contacts the surface of MoS_2, there is no charge transfer due to the stable electronic structure, so it is very difficult to gain and lose electrons, meaning that it cannot play a role in regulating the PL intensity and position[137]. Later, Nan *et al.*[138] demonstrated the reinforced modulation of the PL emission of MoS_2 through chemically bonded O_2 in a mild plasma treatment. Although physical adsorption is a reversible method for quantitatively adjusting the doping concentration through controlling the gas pressure, it cannot meet the requirements for preparing controllable and stable

doping materials due to its poor adsorption ability.

Metal and metal compounds[134], like ion complexes[139] and oxides[140,141], can be applied to decorate the surface of MoS_2. In general, evaporation and solution case methods that are compatible with existing patterning techniques are applied for decorating MoS_2. It has been proved that choosing the dopant sources according to their work function can be used to predict the electrical doping behavior. Sarkar *et al.*[142] studied the electrical doping of MoS_2 via various noble metals, such as Au, Ag, Pd, Pt, Sc and Y. All the metals with large work functions (44.6 eV) were doped into MoS_2. Of these metals, Sc exhibited only a slight depletion effect, while Y induced electron doping behavior with the lowest work function. This phenomenon demonstrates that the dopants with higher work functions have a tendency to act as p-type dopants.

Potassium has a strong ability to supply electrons for most surfaces due to its low electron affinity[143]. Fang *et al.*[134] first reported an n-type-doped thin layer of MoS_2 based on surface charge transfer by depositing potassium atoms on the surface of MoS_2 via vacuum thermal evaporation and controlling the adsorption amount [Figure 22D]. The transfer curve before and after doping [Figure 22E] shows that the device has a large switching ratio (lon/off > 105) before doping. When the channel was completely evaporated of potassium atoms, the source leakage current increased by five orders of magnitude, close to milliamps. Moreover, the source-drain current was almost saturated, indicating the transfer of electrons from potassium to the surface of MoS_2. The surface change density of potassium-doped MoS_2 reached 1.0×10^{13} cm^{-2}. Although the surface charge density of MoS_2 is greatly improved after potassium doping, the current switching ratio significantly decreases. Furthermore, its poor stability limits its practical application, owing to the facile reaction between potassium and O_2 and H_2O.

In addition to potassium, other materials, such as fullerenes (C60) and MoO_3[144], have been doped on the surface of MoS_2. Lin *et al.*[145] researched the effects of C60 and MoO_3 on the surface charge of MoS_2 via vapor methods. Since the lowest unoccupied electrons of the energy level in C60 is higher than the CB of MoS_2, the electron transfer from MoS_2 to C60 is prevented. Furthermore, the p-type doping effect is not produced and the mobility does not decrease, indicating that C60 can be used as an effective protective film. When MoO_3 is used as the covering film, the threshold voltage increases from 0 to 70 eV, indicating that MoO_3 significantly reduces the charge on the surface of MoS_2 and is a suitable p-type dopant. Cs_2CO_3, as an electron injection layer in organic light-emitting diodes, has the ability to provide electrons and produce a strong n-type doping effect on different organic semiconductor materials. Rai *et al.*[146] spin-coated amorphous titanium oxide in a solution-gel state on the surface of MoS_2 and found that the electron mobility was as high as 83 $cm^2 \cdot V^{-1} \cdot s^{-1}$ after doping at room temperature and the intrinsic mobility at 77 K is as high as 501 $cm^2 \cdot V^{-1} \cdot s^{-1}$. Simultaneously, they reported that only when titanium is in excess, amorphous titanium oxide with oxygen holes has the doping effect because the extra Ti atoms can generate additional energy levels at the bottom of the CB.

In addition to the above methods for achieving surface charge transfer based on gas-phase physical adsorption, surface evaporation or spin coating, solution immersion is also a simple and effective method to achieve the adsorption of doped molecules on the surface of MoS_2[147]. Du *et al.*[148] soaked MoS_2 in a methanol solution containing amino-rich polyetherimide. The in-plane and contact resistance decreased from 19.99 and 5.06 $k\Omega \cdot m^{-1}$ to 7.65 and 4.57 $k\Omega \cdot m^{-1}$, respectively. After doping MoS_2, it also has good air stability.

Charge transfer represents a simple and effective doping method to improve the concentration of surface carriers or change the type of carrier in MoS_2. When n-type MoS_2 is doped with an electron-donating dopant, such as an amino group, the electron concentration of the surface of MoS_2 reaches the limit of electron concentration. When patterned p-type doping is carried out with highly electronegative dopants, such as O and F, homogeneous p-n junctions can also be constructed. Compared with substitutional doping, surface adsorption does not destroy the structure of MoS_2 and only transfers the charge; thus, the structure of MoS_2 is more complete. The experimental method of charge transfer doping has also been expanded from gas physical adsorption to solution-phase adsorption, which needs to be further developed in the future to meet the requirements of large-area, controllable, air stable and other practical applications.

Substitutional doping

Substitutional doping involves the replacement of the Mo and S atoms in MoS_2 with cationic and anionic elements of comparable radii[149,150]. After doping, the generation of n- or p-type MoS_2 depends on the number of valence electrons of the dopants. Substitutional doping requires significant energy because of the replacement of heteroatoms for Mo or S atoms and the bonding of heteroatoms with Mo and S atoms around. There are two main methods to realize substitutional doping. One is in-situ doping in the growth process. The other is the creation of vacancies by post-processing, with heteroatoms introduced to fill the vacancies.

Both the bottom-up chemical synthesis and top-down stripping of MoS_2 have S atom holes, so that MoS_2 shows n-type characteristics. If MoS_2 can be doped into a p-type semiconductor, a MoS_2 homojunction will be constructed. In the crystal lattice of MoS_2 [Figure 23A], the Mo atoms are sandwiched between the outer chalcogenide layers, which screens the incorporated metal atoms into the substitutional sites. Non-metal dopants tend to occupy the anionic sites at the outer layers due to the length limitation of the ionic bonds. For metal dopants, the radii of the foreign dopant atoms are vital for a favorable position. For light metals (Li and Na), which have small radii, the interlayer distance (0.615 nm) is sufficient for intercalation. However, for heavy dopants with large radii (e.g., Mn, Co, Zn, and so on), substitutional doping is preferred thermodynamically[149].

At the cation sites, many transition metal ions with similar radii to Mo atoms can achieve effective substitutional doping into the lattice of MoS_2, which enriches its functionality [Figure 23C and D]. In theory, Nb is a very suitable electron acceptor for p-type doping in MoS_2 because it has fewer valence electrons than Mo[151]. From the perspectives of the structures of 2H MoS_2 and 2H NbS_2, the lattice parameters are similar. The covalent radii of r(Mo) (130 pm) and r(Nb) (134 pm) are similar. In terms of oxidation valence states, Mo and Nb are in the 4+ state. Based on the above factors, Nb doping does not cause obvious damage to the original structure of MoS_2. Suh *et al.*[122] prepared millimeter-grade MoS_2 single crystals through chemical vapor phase transport using iodine as a transport agent under a growth temperature gradient of 1050 °C -936 °C for 500 h. Finally, monolayer Nb-doped MoS_2 was obtained by mechanical stripping. Figure 23B shows a schematic of the Nb-doped MoS_2 structure by chemical vapor transport. After doping, the hole concentration reached 1.8×10^{14} cm^{-2}, which is consistent with theoretical calculations that when an Nb atom absorbs an electron, 0.5% Nb atoms can produce a hole density of ~2.8×10^{14} cm^{-2}. Finally, the MoS_2 homojunction was constructed[122]. As seen in the figure of transfer characteristic, the dependence of Nb-doped MoS_2 on the gate decreases and the current increases, presenting p-type doping characteristics [Figure 23E and F]. Different from the above Nb-MoS_2, which was first synthesized in the bulk phase and then obtained as a monolayer by stripping, Laskar *et al.*[152] adopted the method for synthesizing Nb-doped MoS_2 with a thickness of 10 nm by CVD. In terms of doping concentration, the concentration of holes in the bulk phase reached 3.1×10^{20} cm^{-3} and their mobility was 8.5 $cm^2 \cdot V^{-1} \cdot s^{-1}$.

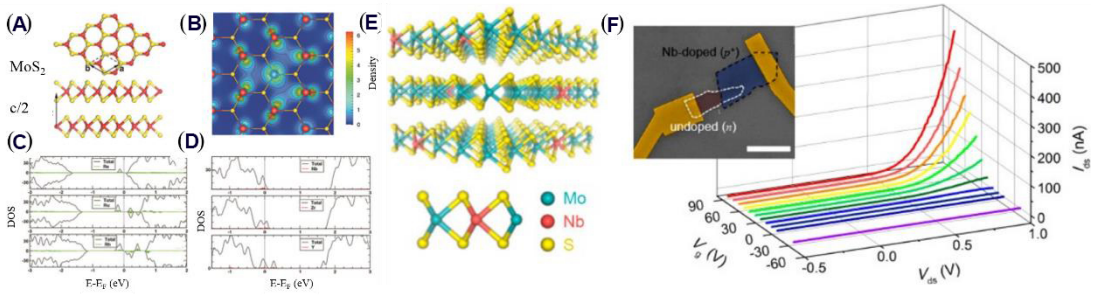

Figure 23. Substitutional doping of MoS_2. Crystal structure of MoS_2 (A). Electron density mapping of MoS_2 with Mo substituted by Nb atom (B). Electronic DOS of Re, Ru and Rh (C) and Nb, Zr and Y substitutionally doped MoS_2 (D)[151]. Structure (E) and electrical properties (F) of Nb-doped MoS_2[122].

In 2016, Gao *et al.*[153] successfully prepared Nb- and Re-doped MoS_2 with a monolayer thickness by direct growth in CVD. The obtained concentration of Re was lower than that of Nb because of the difference in formation energy. In order to make sure whether the dopants were at the substitutional site, aberration-corrected Z-contrast scanning transmission electron microscopy (STEM) was used to observe the position of Nb in the single-layer MoS_2. Furthermore, other indirect methods have been used for detecting the substitutional position. Lin *et al.*[154] investigated the stability of dopants by high electron beam irradiation. On the surface of MoS_2, it was found that Au migrates to the edges and vacancy sites when it possesses sufficient energy from electron irradiation, while the Nb doping results in enhanced stability. The successful substitutional doping in CVD growth enables the turning of electrical conductance. The n-type dopant (Re) greatly reduced the contact resistance in transistors.

The doping of Fe, Mn and other metal atoms may make MoS_2 magnetic, which provides conditions for the preparation of spin devices. It is predicted that the Curie temperature of MoS_2 can exceed room temperature when the Mn content reaches 10%-15%[155]. The chemical bond strength between these dopants and S atoms greatly differs from that of the Mo-S bond, so doping with these atoms may produce lattice defects. Zhang *et al.*[125] studied the influence of the substrate on the doping of Mn atoms. When a substrate with a flat surface was used, such as graphene, trace doping could be carried out at concentrations of < 2%. Higher concentrations led to competition between MoS_2 and MnS, resulting in structural instability. When using substrates with suspended bonds on the surface, like SiO_2/Si and sapphire, doped Mn atoms caused defects in MoS_2. They used molybdenum trioxide as a molybdenum source, heated it to 725 °C in the center of a tubular furnace and placed decarbonyl manganese and sulfur powder in an argon gas inlet and heated them to 70 °C and 300 °C, respectively, for in-situ doping during growth. The morphology of MoS_2 with SiO_2/Si and sapphire substrates before and after the doping of Mn atoms showed that MoS_2 had smooth edges before doping that became serrated after doping.

Because MoS_2 is a sandwich structure, the Mo atom is located in the middle, while the S atoms are located in the upper and lower layers, so the substitution of S atoms can be achieved either by in-situ growth by mixing the doped atoms with the S source or by hole creation by post-laser doping. The substitutional anion doping tends to happen in the presence of anion vacancies exposed to the outer surface. Various doping elements that are available in the gas phase, like H, O, Cl, N and P, can be adopted to reduce the resistance.

Anion substitutional doping depends on the diffusion of dopants to the vacancy sites. Fixed point doping can be accomplished through a laser-assisted doping method. Li *et al.*[156] realized the Se doping of MoS_2 through a CVD method to obtain 2D $MoS_{2x}Se_{2(1-x)}$ with a tuned composition. Ma *et al.*[157] demonstrated that

using Se sources of diselenodiphenyl at about 350°C achieved 21% selenization. Since N-doped MoS_2 can enhance its catalytic hydrogen evolution reaction ability[158], Qin *et al.*[159] prepared gelatinous precursors by dissolving molybdenum pentachloride and thiourea in an ethanol solution with various molar ratios and then placed the gelatinous precursors in a tube furnace. Chen *et al.*[160] etched MoS_2 on the surface of sulfur hexafluoride, trifluoromethane, tetrafluoromethane and O_2, thus obtaining p-type F-doped MoS_2 and constructing a MoS_2 homojunction, which is simpler in structure compared with the traditional heterojunction. The lattice constants between the interfaces were exactly the same. In 2016, Nipane *et al.*[161] doped both non-degenerate and degenerate p-type conductance into MoS_2 via inductively-coupled PH_3:H_2 plasma treatment. The hole mobility in P-doped MoS_2 reached 8.4 and 137 $cm \cdot V^{-1} \cdot s^{-1}$, respectively, after correcting for the contact resistance.

Substitutional doping is important for achieving control of the magnetic and optical properties of MoS_2 and enriching the diversity of its composition. Because excessive Mo or S atoms in substituted MoS_2 will destroy the stability of its structure, substitutional doping is not the main method to control the electron concentration. The homogenous distribution of impurity atoms can be obtained by central doping in the growth process of MoS_2, while the laser-assisted method can realize the fixed point doping of dopants. The doping concentration can be controlled by adjusting the laser intensity and exposure time. This method provides a new concept for the construction of homojunctions.

Intercalation doping

Unlike substitutional doping, the van der Waals interlayer of MoS_2 allows for foreign ion intercalation[162] and atoms[163] and also molecules to enter into the interlayer space. Intercalation is beneficial for the exfoliation of MoS_2 in solution in order to produce novel batteries and electrochemical cells[63,164]. Intercalation doping can modulate the electronic structure and crystal lattice of the supporting materials, resulting in physical or chemical phenomena, including charge density and superconductivity.

H and alkali metal ions can be very easily intercalated into the intercalation layers due to their small radii[165]. Furthermore, they induce electronic structure changes and lattice distortion due to the reductive nature by donating electrons to the lattice. At room temperature, the stable crystal structure of MoS_2 is 2H, i.e., six S atoms are coordinated around Mo atoms to form a trigonal prism coordination environment. In this coordination environment, the 4d orbital of the central Mo ion is divided into three groups and the two 4d electrons of the tetravalent Mo ions are arranged in the lowest orbital, which keeps the system with the highest stability. However, after interlayer doping with alkali metals, the coordination environment of the central Mo ion is changed into the octahedral 1T configuration for maintaining the lowest energy electron configuration. This is because the alkali metal injects more electrons into MoS_2 and the 4d orbital is separated into two groups. The newly injected electrons are arranged with the original two electrons in the lowest energy dxy, dyz and dxz parallel rails. Therefore, the intercalation doping of alkali metal ions brings changes in the crystal structure of MoS_2. It was seen that the injection of electrons changes the electrical properties of MoS_2 according to the distribution diagram of state density before and after doping. The Fermi level has the distribution of state density, which makes MoS_2 change from a semiconducting to a metal state[166].

Alkali metal intercalation is mainly achieved through the immersion of a butyl solution or electrochemical method. Lukowski *et al.*[167] synthesized petal-like multilayer MoS_2 with highly exposed edge sites on a graphene substrate by CVD, then soaked the multilayer petal-like MoS_2 in an n-butyl lithium solution for 6-8 h and finally removed it with deionized water to remove the excess Li. Acerce *et al.*[168] prepared 1T MoS_2 with a size of 1-5 μm by first making MoS_2 into a single layer and then stacking it. MoS_2 powder was first

soaked in an n-butyl lithium solution, filtered through argon for 48 h and the excess butyl lithium solution was washed away with hexane, before finally soaking the Li-intercalated MoS_2 in deionized water and ultrasound for 1 h to wash away the Li interlayer and obtain the single-layer MoS_2.

The zerovalent intercalation of heavy metal elements, such as Co, Cu and so on, can be intercalated into the intercalation layers[169-171]. This avoids lattice disruption without a charge interaction between the doping atoms and supporting materials. It was demonstrated that various organic molecules with different functional groups can facilitate the origination of new intercalation systems with engineered enhanced functions, including ferromagnetic moments[172], charge density waves and superconductivity[173]. Chen *et al.*[174] successfully synthesized the intercalation doping of Pt, Ru, Au and Pd in highly reductive 1T' Li_xMoS_2 by the in-situ reduction of metal ions. In the process, Li^+ intercalation enlarges the van der Waal gap in 1T' Li_xMoS_2, which allows the diffusion of highly charged metal ions ($PbCl_6^{2-}$, Ru^{3+}, $AuCl_4^-$ and Pb^{2+}) into the interlayer space. After in-situ reduction, the noble metal particles are precipitated in the interlayer space. Li^+ and Cl^- are leached out through ion exchange, the zerovalent intercalated MoS_2 is restored to the 2H phase. The zerovalent is kept in the stable 2H structure. The encapsulation of noble metal clusters in MoS_2 is used for stability in catalytic applications. In addition to the above-mentioned ions and elemental atoms with small sizes, large molecules can also be applied as intercalants. The organic molecules as intercalation dopants facilitate the discovery of new intercalation systems and engineering owing to their enormous functional groups.

Composites

Composite construction with single elements

Although its special microstructure and proper bandgap structure endow MoS_2 with excellent physical properties and chemical activity, its properties can be further optimized by constructing composites with single elements. Noble metals are the most common elements used to modify MoS_2 for superconductivity and special surface plasmon resonance. Through some techniques, noble metal nanoparticles can be anchored on MoS_2 to form composites[175]. According to Sun *et al.*[176], MoS_2 decorated with Ag^0 could be successfully prepared by reducing $AgNO_3$ on MoS_2. As a result, Ag^0 dramatically facilitated the delivery of photogenerated electrons from MoS_2, leading to an improvement in the photocatalytic efficiency for Cr(VI) reduction. In another study, Ag/MoS_2 was fabricated as a Fenton catalyst. Under the irradiation of light, "hot electrons" generated by the surface plasmon resonance effect of Ag^0 can facilitate the separation of electron-hole pairs to co-catalyze Fenton reaction, thus improving the degradation of 2,4-dichlorophenol[177]. As another kind of noble metal, Au is popular in the modification on MoS_2 to regulate the surface structure. Yin *et al.*[178] loaded Au nanoparticles on MoS_2 to improve the photocatalytic features. After Au decoration, the photocurrent response increased from 100 to 370 μA cm^{-2} at 0.8 V (*vs.* Ag/AgCl), ascribed to the local electric field generated by Au. As well as Ag and Au, other common noble metals, such as Pt and Pd, have also been used to decorate MoS_2. Luo *et al.*[179] adopted an electrodeposition method to import Pt on MoS_2 and it exhibited a comparable HER activity. As reported by Yuwen *et al.*[175], they utilized a microwave-assisted method to disperse Pd on MoS_2, leading to an enhanced catalytic activity for methanol oxidation.

Some heavy metal elements have also been adopted to construct composites with MoS_2 in the lubrication and advanced oxidation process fields. Sun *et al.*[180] induced Cu atoms into MoS_2 to form a turbulence-like micro-nanostructured composite (Cu/MoS_2) and utilized it as a solid lubricant. With the introduction of Cu, the composite exhibited higher hardness and a lower friction coefficient in the atmosphere than pure MoS_2. The Fenton reaction is considered a promising technique among various advanced oxidation processes. In the report of Lan *et al.*[181], isolated protruding Fe atoms were immobilized on MoS_2 surface through a dipping calcination method to prepare a Fenton catalyst (Fe-MoS_2). During the piezo-activation

of peroxymonosulfate, the isolated Fe atomic sites play important roles in promoting the separation of e^- and h^+ of MoS_2, as well as providing Fe^{2+} for peroxymonosulfate decomposition.

Heterojunctions

The photoactivity of MoS_2 can be enhanced through appropriate heterojunction engineering for inhibiting the recombination of induced photoelectrons and holes. According to the contact interface, heterojunctions can be divided into six groups [Figure 24]: traditional (types I, II and III); p-n; Z-scheme; step-scheme; Schottky and surface heterojunctions[182-184]. The diverse heterojunction structure shows different methods and mechanisms for the transfer of photogenerated carriers.

In type I heterojunction photocatalysts [Figure 24A], both photogenerated electrons and holes flow from the higher conduction and lower valence bands to another semiconductor. Nevertheless, type I heterojunctions cannot easily separate charge carriers, resulting in the accumulation of electrons and holes in one semiconductor[185]. Type II heterojunctions effectively avoid the accumulation problems [Figure 24B], as the electrons transfer to the semiconductor with a lower CB and holes transfer with a higher VB, thus decreasing the contact and recombination of electron-hole pairs[186]. Although the structure of type III heterojunctions [Figure 24C] is close to the type II structure, the bandgap of each does not overlap due to the extreme levels of the bands[187]. In a traditional heterojunction, only type II heterojunctions possess an ideal structure for improving the separation of electron-hole pairs.

Taking the example of CdS/MoS_2[188], a type I heterojunction, the photogenerated electrons in the CB of CdS transfer to the CB of MoS_2 due to the more positive conduction of MoS_2 than that of CdS. Therefore, photogenerated electron-hole pairs will be separated in CdS and then enhance the catalytic activity. However, simultaneously, the holes transfer from the VB of CdS to that of MoS_2. Both electrons and holes accumulate in MoS_2, resulting in the ineffective separation in the type I CdS/MoS_2 heterojunction. For a type II heterojunction, like $MoS_2/g\text{-}C_3N_4$[189], the photogenerated electrons transfer from the CB of $g\text{-}C_3N_4$ to the CB of MoS_2, while the holes move in the opposite direction. As a result, electrons and holes are separated and accumulated in MoS_2 and $g\text{-}C_3N_4$, respectively. The separation of charge carriers can significantly reduce the recombination of charges and achieve high catalytic activity.

Because of the diffusion of carriers between semiconductors, there exists an internal electric field on the interface between p- and n-type semiconductors [Figure 24D][190,191]. In the electric field, the electrons and holes will be quickly driven to the CB of the n-type semiconductor and the VB of the p-type semiconductor, respectively. Thus, electrons and holes will be finally separated in the presence of the internal electric field in a p-n heterojunction system. For example, Meng *et al.*[38] synthesized a p-n heterojunction ($p\text{-}MoS_2/n\text{-}Bi_2WO_6$) through a bath sonication method. Electrons on $n\text{-}Bi_2WO_6$ transfer into the $p\text{-}MoS_2$, while holes on $p\text{-}MoS_2$ move in the opposite direction, thus resulting in a built-in electric field forming at the interface. With the illumination, electrons and holes will be separated quickly via the synergetic effect and fast charge recombination will be efficiently inhibited simultaneously. All the heterojunction catalysts show high separation efficiency of photogenerated electron-hole pairs.

There are three types (traditional, all-solid-state and direct Z-scheme) of Z-scheme heterojunctions. In the structures, the charge transfer method is similar but with no intermediate[192,193]. In a direct Z-scheme catalyst, recombination occurs between weak electrons with less negative CB and holes from the semiconductor with less positive VB [Figure 24E]. As a result, the high oxidation holes and reduction electrons cannot recombine and be maintained for catalytic reactions[194,195]. This method gives new insights into the enhancement of catalytic activity by consuming the excess electrons and holes for the remaining

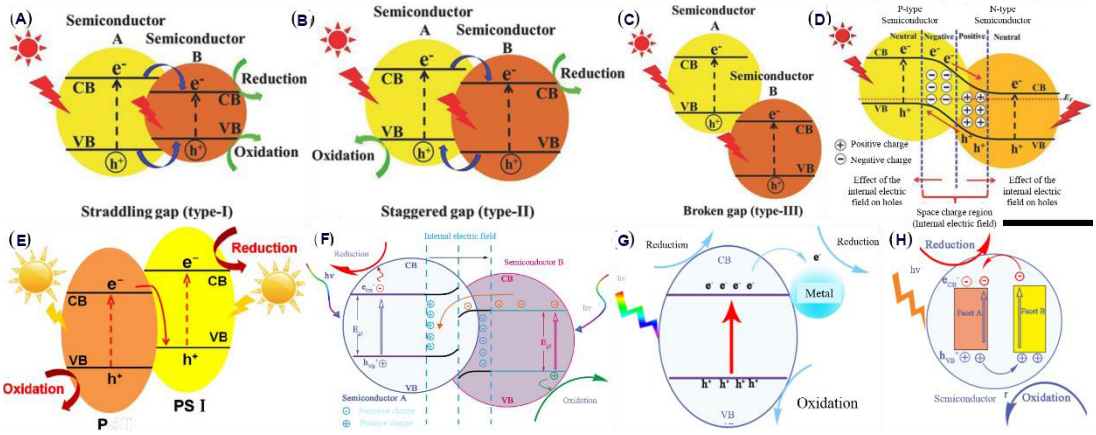

Figure 24. Schematic of band structure and charge carrier transfer of traditional heterojunction systems (A-C), a p-n heterojunction system (D)[191], a direct Z-scheme heterojunction system (E)[194], a step scheme heterojunction system (F)[201], a Schottky junction system (G)[204] and a surface heterojunction system (H)[205].

high redox potential in the system. Xiong *et al.*[196] prepared a Z-scheme heterojunction, $(BiO)_2CO_3/MoS_2$, for the removal of NO 44. Under irradiation, both $(BiO)_2CO_3$ and MoS_2 generated electron-hole pairs. The photogenerated electrons in the CB of $(BiO)_2CO_3$ diffused and combined with the holes in the VB of MoS_2. After that, electrons and holes will be separated and then accumulated at the CB of MoS_2 and the VB of $(BiO)_2CO_3$, respectively. In addition, ternary heterojunctions are also effective architectures for improving the catalytic activity of binary structures. Zhang *et al.*[197] synthesized a ternary nanocomposite, TiO_2/g-C_3N_4 /MoS_2, which exhibited two type II heterojunctions at the interface of TiO_2/g-C_3N_4 and TiO_2/MoS_2. Photogenerated electrons will transfer from the CB of g-C_3N_4 (or MoS_2) to the CB of TiO_2. Furthermore, the photogenerated holes in the VB of TiO_2 shift to the VB of g-C_3N_4 (or MoS_2). Finally, TiO_2 will receive the most photogenerated electrons, which reduce the O_2 and $\bullet O^{2-}$ for degradation. In contrast, g-C_3N_4 and MoS_2 collect the main photogenerated holes. According to previous reports, TiO_2/g-C_3N_4 with the addition of MoS_2 has higher catalytic activity than that without MoS_2 because of the existence of a synergetic effect between TiO_2/g-C_3N_4 and TiO_2/MoS_2 heterojunctions. Beyond that, TiO_2/g-C_3N_4/MoS_2 composite not only extends the light absorption ability but also enhances the light utilization rate. Other ternary catalysts with MoS_2 possess advanced performance.

The step-scheme system is composed of two n-type semiconductors with a staggered band structure, which is similar to type II except for the path of charge migration [Figure 24F][198-201]. An electric field is generated from semiconductor A with a greater work function and lower Fermi level to the one (semiconductor B) with smaller work function and higher Fermi level because of the spontaneous diffusion of electrons on the interface. In addition, electron donors will bend upward owing to electron depletion, and another conductor does the opposite with downward bending originating from the electron accumulation[202]. Therefore, the electrons in semiconductor B will combine with oxidative holes from semiconductor A, which is similar to the Z-scheme heterostructure. Schottky heterojunctions are generated with an interaction between a semiconductor and a metal [Figure 24G][203,204]. The electrons are transferred from metal to semiconductor, owing to their different Fermi energies. As for surface heterojunctions, they mainly consist of two different crystal facets of a single semiconductor[205,206]. The mechanism regarding separation of carriers in the surface heterojunction is similar to that in type II [Figure 24H][207]. However, the redox potential in surface heterojunctions is lower than that in type II heterojunctions.

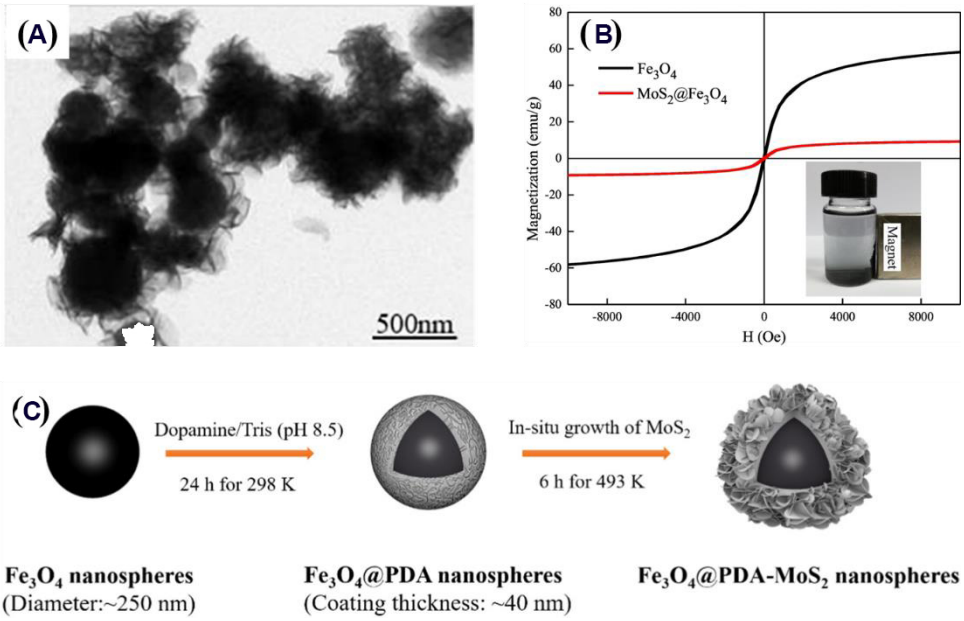

Figure 25. TEM image of MoS_2@ Fe_3O_4 composite (A). Magnetic hysteresis loop of Fe_3O_4 nanospheres and $MoS_2@Fe_3O_4$ composite (B). Fabrication procedure of Fe_3O_4@PDA-MoS_2 nanosphere (C)[211,212].

Composite construction with other materials

With increased research, scientists have gradually recognized that pure MoS_2 nanosheets do not meet practical requirements because of their poor conductivity, difficult recovery and low chemical stability[78,112,208]. As a result, various kinds of functional materials have emerged and been researched in recent years as potential hybrids with MoS_2 to solve these challenges.

Polydopamine (PDA) can be synthesized through a self-polymerization method of dopamine by a simple surface coating in an aqueous solution. As a result of its strong surface adhesion, PDA can adhere well onto almost all inorganic and organic materials. Importantly, the stability can be improved after PDA wrapping, according to the literature[209]. For the enhancement of MoS_2 chemical stability, Wang *et al.*[210] coated PDA on MoS_2 to fabricate a MoS_2@PDA composite as a catalyst to recover $AuCl_4^-$. As a result, MoS_2@PDA not only exhibits extraordinary performance in catalysis but also shows strong chemical stability for practical applications.

In order to facilitate the separation of MoS_2 from water for further utilization, it is a common strategy to magnetize MoS_2. Sun *et al.*[211] constructed Fe_3O_4 on MoS_2 to fabricate a core-shell structured $MoS_2@Fe_3O_4$ composite [Figure 25A]. As shown in Figure 25B, this material shows stronger magnetism than pure Fe_3O_4 that can be easily separated from water by a magnet. Furthermore, the MoS_2 component plays the original role, such as the properties of adsorption and exhibited extraordinary effect in recovering gold. Furthermore, Wang *et al.*[212] fabricated a ternary composite of Fe_3O_4@PDA-MoS_2 nanospheres [Figure 25C]. This material not only provides a convenient way to separate material from water by a magnet, but also possesses enough chemical stability, thereby promoting its application as an adsorbent for Pb^{2+} removal. In summary, such MoS_2-based nanocomposites combine the merits of both MoS_2 nanosheets and functional materials, promoting the applications progress of MoS_2-based nanocomposites in the relevant fields.

CONCLUSION AND OUTLOOK

This review has provided an overview on the strategies and recent advances towards the synthesis, modification and application of 0D, 2D and 3D MoS_2. It has been demonstrated that 0D, 2D and 3D MoS_2 are very promising for many applications in the fields of water treatment, energy storage and conversion, biology and optoelectronics because of their special properties, including non-toxicity, optical, semiconducting and layer structure properties. The methods for synthesizing 0D, 2D and 3D MoS_2, including liquid exfoliation, electrochemical, template-based, self-assembly and sol-gel and hydrothermal methods, are widely researched. However, the main challenging issue remains the usage of 0D, 2D and 3D MoS_2 is the efficient and low-cost preparation with high quality. An attempt to overcome this issue will drive force for the development of 0D, 2D and 3D MoS_2 for applications.

Furthermore, this review focuses on the modification methods, including surface defects, heteroatom doping and composites for turning the structure and improving the ability of 0D, 2D and 3D MoS_2. Until now, point-like and plane like defects engineering, charge transfer doping, substitutional doping, intercalation doping, composite with elemental, heterojunction and other materials are adopted for both the non-degenerate and degenerate modulation of MoS_2. This not only enables the realization of widely tuned physical and chemical properties but also allows the appearance of metallic behaviors and phase transition under intensive charge injection. Nevertheless, there are still challenges mainly arising from the requirements of addressing the precisely controlled properties, expensive, activation and long-term stability issues, and also the performance. Every method has its own limitations and properties, which greatly improve the development of MoS_2. Moreover, optimizing existing or finding methods is still vital for improving the performance and application of 0D, 2D and 3D MoS_2.

Hence, it is concluded that when advanced synthetic methods satisfy the applications, 0D, 2D and 3D MoS_2 would be realized in various fields, such as electronics, optoelectronics, environmental and energy technologies. In conclusion, the modification strategies of 0D, 2D and 3D MoS_2 and their potential applications have been reviewed. There is immense worth in realizing the application potential of MoS_2.

DECLARATIONS

Authors' contributions

Writing (Abstract, Introduction, Chapter 3.2, 3.3.2, Conclusion and outlook); Review; Editing: Zhan W
Writing (Structural Property): Yuan Y
Writing (Chapter 3.1, 3.3.1 and 3.3.3): Liu C
Writing (Chapter 2.3): Chen P
Writing (Chapter 2.1): Liang Y
Writing (Chapter 2.2): Wang Y
Validation: Arauz-Lara JL
Suspension, data curation, formal analysis: Jia F

Availability of data and materials

Not applicable.

Ethical approval and consent to participate

Not applicable.

Consent for publication

Not applicable.

Financial support and sponsorship

Not applicable.

Conflicts of interest

All authors declared that there are no conflicts of interest.

REFERENCES

1. Pető J, Ollár T, Vancsó P, et al. Spontaneous doping of the basal plane of MoS_2 single layers through oxygen substitution under ambient conditions. *Nat Chem* 2018;10:1246-51. DOI PubMed
2. Yuan Y, Guo R, Hong L, et al. Recent advances and perspectives of MoS_2-based materials for photocatalytic dyes degradation: a review. *Colloids and Surfaces A: Physicochemical and Engineering Aspects* 2021;611:125836. DOI
3. Liu G, Robertson AW, Li MM, et al. MoS_2 monolayer catalyst doped with isolated Co atoms for the hydrodeoxygenation reaction. *Nat Chem* 2017;9:810-6. DOI PubMed
4. Yuan Y, Yang B, Jia F, Song S. Reduction mechanism of Au metal ions into Au nanoparticles on molybdenum disulfide. *Nanoscale* 2019;11:9488-97. DOI PubMed
5. Xia D(, Gong F, Pei X, et al. Molybdenum and tungsten disulfides-based nanocomposite films for energy storage and conversion: a review. *Chemical Engineering Journal* 2018;348:908-28.
6. Zhang J, Wang T, Liu P, et al. Engineering water dissociation sites in MoS_2 nanosheets for accelerated electrocatalytic hydrogen production. *Energy Environ Sci* 2016;9:2789-93.
7. Zhu H, Gan X, Mccreary A, Lv R, Lin Z, Terrones M. Heteroatom doping of two-dimensional materials: from graphene to chalcogenides. *Nano Today* 2020;30:100829.
8. Ge J, Ou EC, Yu RQ, Chu X. A novel aptameric nanobiosensor based on the self-assembled DNA-MoS_2 nanosheet architecture for biomolecule detection. *J Mater Chem B* 2014;2:625-8. DOI PubMed
9. Wu J, Zhang X, Ma X, Qiu Y, Zhang T. High quantum-yield luminescent MoS_2 quantum dots with variable light emission created via direct ultrasonic exfoliation of MoS_2 nanosheets. *RSC Adv* 2015;5:95178-82.
10. Wang Y, Ni Y. Molybdenum disulfide quantum dots as a photoluminescence sensing platform for 2,4,6-trinitrophenol detection. *Anal Chem* 2014;86:7463-70. DOI PubMed
11. Dai W, Dong H, Fugetsu B, et al. Tunable fabrication of molybdenum disulfide quantum dots for intracellular microRNA detection and multiphoton bioimaging. *Small* 2015;11:4158-64. DOI PubMed
12. Ali J, Siddiqui GU, Choi KH, Jang Y, Lee K. Fabrication of blue luminescent MoS_2 quantum dots by wet grinding assisted co-solvent sonication. *Journal of Luminescence* 2016;169:342-7.
13. Dong H, Tang S, Hao Y, et al. Fluorescent MoS_2 quantum dots: ultrasonic preparation, up-conversion and down-conversion bioimaging, and photodynamic therapy. *ACS Appl Mater Interfaces* 2016;8:3107-14. DOI PubMed
14. Xu S, Li D, Wu P. One-pot, facile, and versatile synthesis of monolayer MoS_2/WS_2 quantum dots as bioimaging probes and efficient electrocatalysts for hydrogen evolution reaction. *Adv Funct Mater* 2015;25:1127-36.
15. Wang N, Wei F, Qi Y, et al. Synthesis of strongly fluorescent molybdenum disulfide nanosheets for cell-targeted labeling. *ACS Appl Mater Interfaces* 2014;6:19888-94. DOI PubMed
16. Qiao W, Yan S, Song X, et al. Monolayer MoS_2 quantum dots as catalysts for efficient hydrogen evolution. *RSC Adv* 2015;5:97696-701.
17. Zhang H. Ultrathin two-dimensional nanomaterials. *ACS Nano* 2015;9:9451-69. DOI PubMed
18. Ataca C, Şahin H, Ciraci S. Stable, Single-layer MX_2 transition-metal oxides and dichalcogenides in a honeycomb-like structure. *J Phys Chem C* 2012;116:8983-99. DOI
19. Eda G, Yamaguchi H, Voiry D, Fujita T, Chen M, Chhowalla M. Photoluminescence from chemically exfoliated MoS2. *Nano Lett* 2011;11:5111-6. DOI PubMed
20. Mak KF, Lee C, Hone J, Shan J, Heinz TF. Atomically thin MoS_2: a new direct-gap semiconductor. *Phys Rev Lett* 2010;105:136805. DOI
21. Kuc A, Zibouche N, Heine T. Influence of quantum confinement on the electronic structure of the transition metal sulfide T S 2. *Phys Rev B* 2011:83. DOI
22. Splendiani A, Sun L, Zhang Y, et al. Emerging photoluminescence in monolayer MoS2. *Nano Lett* 2010;10:1271-5. DOI PubMed
23. Ataca C, Ciraci S. Functionalization of single-layer MoS_2 honeycomb structures. *J Phys Chem C* 2011;115:13303-11. DOI

24. Mann J, Sun D, Ma Q, et al. Facile growth of monolayer MoS_2 film areas on SiO2. *Eur Phys J B* 2013:86.
25. Kadantsev ES, Hawrylak P. Electronic structure of a single MoS_2 monolayer. *Solid State Communications* 2012;152:909-13.
26. Ramasubramaniam A. Large excitonic effects in monolayers of molybdenum and tungsten dichalcogenides. *Phys Rev B* 2012:86.
27. Bertolazzi S, Brivio J, Kis A. Stretching and breaking of ultrathin MoS_2. *ACS Nano* 2011;5:9703-9. DOI PubMed
28. Duerloo KN, Ong MT, Reed EJ. Intrinsic piezoelectricity in two-dimensional materials. *J Phys Chem Lett* 2012;3:2871-6.
29. Tiras E, Ardali S, Tiras T, et al. Effective mass of electron in monolayer graphene: electron-phonon interaction. *Journal of Applied Physics* 2013;113:043708.
30. Feng J, Qian X, Huang C, Li J. Strain-engineered artificial atom as a broad-spectrum solar energy funnel. *Nature Photon* 2012;6:866-72. DOI
31. Zhang L, Wu HB, Yan Y, Wang X, Lou XW. Hierarchical MoS_2 microboxes constructed by nanosheets with enhanced electrochemical properties for lithium storage and water splitting. *Energy Environ Sci* 2014;7:3302-6. DOI
32. Liu N, Guo Y, Yang X, et al. Microwave-assisted reactant-protecting strategy toward efficient MoS_2 electrocatalysts in hydrogen evolution reaction. *ACS Appl Mater Interfaces* 2015;7:23741-9. DOI PubMed
33. Li BL, Setyawati MI, Zou HL, et al. Emerging 0D Transition-metal dichalcogenides for sensors, biomedicine, and clean energy. *Small* 2017;13:1700527. DOI PubMed
34. Guo Y, Li J. MoS_2 quantum dots: synthesis, properties and biological applications. *Mater Sci Eng C Mater Biol Appl* 2020;109:110511. DOI PubMed
35. Zhang W, Du J, Liu Z, et al. Production of carbon dots during the liquid phase exfoliation of MoS2 quantum dots. *Carbon* 2019;155:243-9. DOI
36. Gopalakrishnan D, Damien D, Shaijumon MM. MoS_2 quantum dot-interspersed exfoliated MoS2 nanosheets. *ACS Nano* 2014;8:5297-303. DOI PubMed
37. Wang T, Liu L, Zhu Z, et al. Enhanced electrocatalytic activity for hydrogen evolution reaction from self-assembled monodispersed molybdenum sulfidenanoparticles on an Au electrode. *Energy Environ Sci* 2013;6:625-33. DOI
38. Meng X, Li Z, Zeng H, Chen J, Zhang Z. MoS_2 quantum dots-interspersed Bi_2WO_6 heterostructures for visible light-induced detoxification and disinfection. *Applied Catalysis B: Environmental* 2017;210:160-72. DOI
39. Gopalakrishnan D, Damien D, Li B, et al. Electrochemical synthesis of luminescent MoS_2 quantum dots. *Chem Commun (Camb)* 2015;51:6293-6. DOI PubMed
40. Cao X, Ding C, Zhang C, et al. Transition metal dichalcogenide quantum dots: synthesis, photoluminescence and biological applications. *J Mater Chem B* 2018;6:8011-36. DOI PubMed
41. Shrivastava M, Kumari R, Parra MR, Pandey P, Siddiqui H, Haque FZ. Electrochemical synthesis of MoS_2 quantum dots embedded nanostructured porous silicon with enhanced electroluminescence property. *Optical Materials* 2017;73:763-71. DOI
42. Li BL, Chen LX, Zou HL, Lei JL, Luo HQ, Li NB. Electrochemically induced Fenton reaction of few-layer MoS_2 nanosheets: preparation of luminescent quantum dots via a transition of nanoporous morphology. *Nanoscale* 2014;6:9831-8. DOI PubMed
43. Qiao W, Yan S, Song X, et al. Luminescent monolayer MoS_2 quantum dots produced by multi-exfoliation based on lithium intercalation. *Applied Surface Science* 2015;359:130-6. DOI
44. Grayfer ED, Kozlova MN, Fedorov VE. Colloidal 2D nanosheets of MoS_2 and other transition metal dichalcogenides through liquid-phase exfoliation. *Adv Colloid Interface Sci* 2017;245:40-61. DOI PubMed
45. An S, Park DY, Lee C, et al. Facile preparation of molybdenum disulfide quantum dots using a femtosecond laser. *Applied Surface Science* 2020;511:145507. DOI
46. Ren X, Pang L, Zhang Y, Ren X, Fan H, Liu S. One-step hydrothermal synthesis of monolayer MoS_2 quantum dots for highly efficient electrocatalytic hydrogen evolution. *J Mater Chem A* 2015;3:10693-7. DOI
47. Mohanty B, Ghorbani-asl M, Kretschmer S, et al. MoS_2 quantum dots as efficient catalyst materials for the oxygen evolution reaction. *ACS Catal* 2018;8:1683-9. DOI
48. Gan X, Zhao H, Quan X. Two-dimensional MoS_2: a promising building block for biosensors. *Biosens Bioelectron* 2017;89:56-71. DOI PubMed
49. Li H, Wu J, Yin Z, Zhang H. Preparation and applications of mechanically exfoliated single-layer and multilayer MoS_2 and WSe_2 nanosheets. *Acc Chem Res* 2014;47:1067-75. DOI
50. Yin Z, Li H, Li H, et al. Single-layer MoS2 phototransistors. *ACS Nano* 2012;6:74-80. DOI PubMed
51. Ghatak S, Pal AN, Ghosh A. Nature of electronic states in atomically thin MoS_2 field-effect transistors. *ACS Nano* 2011;5:7707-12. DOI
52. Ciesielski A, Samorì P. Graphene via sonication assisted liquid-phase exfoliation. *Chem Soc Rev* 2014;43:381-98. DOI PubMed
53. Tang Z, Wei Q, Guo B. A generic solvent exchange method to disperse MoS_2 in organic solvents to ease the solution process. *Chem Commun (Camb)* 2014;50:3934-7. DOI PubMed
54. Li Y, Yin X, Wu W. Preparation of few-layer MoS_2 nanosheets via an efficient shearing exfoliation method. *Ind Eng Chem Res* 2018;57:2838-46. DOI
55. Gupta A, Arunachalam V, Vasudevan S. Water dispersible, positively and negatively charged MoS_2 Nanosheets: surface chemistry and the role of surfactant binding. *J Phys Chem Lett* 2015;6:739-44. DOI PubMed
56. Guardia L, Paredes JI, Rozada R, Villar-rodil S, Martínez-alonso A, Tascón JMD. Production of aqueous dispersions of inorganic graphene analogues by exfoliation and stabilization with non-ionic surfactants. *RSC Adv* 2014;4:14115-27. DOI

57. Liu Y, Ren L, Qi X, et al. Preparation, characterization and photoelectrochemical property of ultrathin MoS_2 nanosheets via hydrothermal intercalation and exfoliation route. *Journal of Alloys and Compounds* 2013;571:37-42.
58. Joensen P, Frindt R, Morrison S. Single-layer MoS_2. *Materials Research Bulletin* 1986;21:457-61. DOI
59. Yeon C, Yun SJ, Yang J, Youn DH, Lim JW. Na-cation-assisted exfoliation of MX_2 (M = Mo, W; X = S, Se) Nanosheets in an Aqueous medium with the aid of a polymeric surfactant for flexible polymer-nanocomposite memory applications. *Small* 2018;14:1702747. DOI PubMed
60. Yu H, Zhu H, Dargusch M, Huang Y. A reliable and highly efficient exfoliation method for water-dispersible MoS_2 nanosheet. *J Colloid Interface Sci* 2018;514:642-7. DOI PubMed
61. Lee SK, Chu D, Song DY, Pak SW, Kim EK. Electrical and photovoltaic properties of residue-free MoS_2 thin films by liquid exfoliation method. *Nanotechnology* 2017;28:195703. DOI PubMed
62. You X, Liu N, Lee CJ, Pak JJ. An electrochemical route to MoS_2 nanosheets for device applications. *Materials Letters* 2014;121:31-5.
63. Zeng Z, Yin Z, Huang X, et al. Single-layer semiconducting nanosheets: high-yield preparation and device fabrication. *Angew Chem* 2011;123:11289-93. DOI PubMed
64. Chen F, Jiang X, Shao J, Fu L, Zhao S, Su W. The synthesis and identification of complete stacking bilayer MoS_2 flakes with unconventional shapes via chemical vapor deposition. *Superlattices and Microstructures* 2021;158:107023.
65. Pondick JV, Woods JM, Xing J, Zhou Y, Cha JJ. Stepwise sulfurization from MoO_3 to MoS_2 via chemical vapor deposition. *ACS Appl Nano Mater* 2018;1:5655-61.
66. Perkgoz NK, Bay M. Investigation of single-wall MoS_2 monolayer flakes grown by chemical vapor deposition. *Nanomicro Lett* 2016;8:70-9. DOI PubMed PMC
67. Chowdhury S, Roy A, Liu C, et al. Two-step growth of uniform monolayer MoS_2 nanosheets by metal-organic chemical vapor deposition. *ACS Omega* 2021;6:10343-51. DOI PubMed PMC
68. Liu L, Qiu H, Wang J, Xu G, Jiao L. Atomic MoS_2 monolayers synthesized from a metal-organic complex by chemical vapor deposition. *Nanoscale* 2016;8:4486-90. DOI PubMed
69. Fei L, Lei S, Zhang WB, et al. Direct TEM observations of growth mechanisms of two-dimensional MoS_2 flakes. *Nat Commun* 2016;7:12206. DOI PubMed PMC
70. Lee S, Son Y, Choi J, Kim S, Park S. Morphology and catalytic performance of MoS_2 hydrothermally synthesized at various pH values. *Catalysts* 2021;11:1229.
71. Song T, Fu L, Wan N, Wu J, Xie J. Hydrothermal synthesis of MoS_2 nanoflowers for an efficient microbial electrosynthesis of acetate from CO_2. ;41:101231. DOI
72. Wu D, Zhang C, Xu S, et al. Fabrication and enhanced supercapacitance of hollow nanostructured MoS_2 prepared by a CATB-assisted hydrothermal process. *Materials Letters* 2016;184:96-9. DOI
73. Huang Z, Qi Y, Yu D, Zhan J. Radar-like MoS_2 nanoparticles as a highly efficient 808 nm laser-induced photothermal agent for cancer therapy. *RSC Adv* 2016;6:31031-6. DOI
74. Chen J, Xu Z, Hu Y, Yi M. PEG-assisted solvothermal synthesis of MoS_2 nanosheets with enhanced tribological property. *Lubrication Science* 2020;32:273-82. DOI
75. Wang Q, Jia F, Huang A, et al. MoS_2@sponge with double layer structure for high-efficiency solar desalination. *Desalination* 2020;481:114359. DOI
76. Chen P, Zeng S, Zhao Y, Kang S, Zhang T, Song S. Synthesis of unique-morphological hollow microspheres of MoS_2 @montmorillonite nanosheets for the enhancement of photocatalytic activity and cycle stability. *Journal of Materials Science & Technology* 2020;41:88-97. DOI
77. Zhu L, Ji J, Liu J, et al. Designing 3D-MoS_2 Sponge as excellent cocatalysts in advanced oxidation processes for pollutant control. *Angew Chem* 2020;132:14072-80. DOI PubMed
78. Sun K, Mao S, Zhan W, Liu C, Jia F, Song S. In-situ reduction of $Au(S_2O_3)_{23}$- for efficient recovery of gold with magnetically separable shell-core structured MoS_2@Fe_3O_4 composite. *Hydrometallurgy* 2020;198:105514. DOI
79. Zhang Y, Zuo L, Huang Y, et al. In-situ growth of few-layered MoS_2 nanosheets on highly porous carbon aerogel as advanced electrocatalysts for hydrogen evolution reaction. *ACS Sustainable Chem Eng* 2015;3:3140-8. DOI
80. Xie Y, Guo F, Mao J, et al. Freestanding MoS_2@carbonized cellulose aerogel derived from waste cotton for sustainable and highly efficient particulate matter capturing. *Separation and Purification Technology* 2021;254:117571. DOI
81. Kim K, Tiwari AP, Hyun G, Novak TG, Jeon S. Improving electrochemical active area of MoS_2 via attached on 3D-ordered structures for hydrogen evolution reaction. *International Journal of Hydrogen Energy* 2019;44:28143-50. DOI
82. Wang W, Yang P, Jian Z, Li H, Xing Y, Zhang S. Rational design of a 3D MoS_2/dual-channel graphene framework hybrid as a free-standing electrode for enhanced lithium storage. *J Mater Chem A* 2018;6:13797-805. DOI
83. Xiang Z, Zhang Z, Xu X, Zhang Q, Yuan C. MoS_2 nanosheets array on carbon cloth as a 3D electrode for highly efficient electrochemical hydrogen evolution. *Carbon* 2016;98:84-9. DOI
84. Geng H, Zhang X, Xie W, et al. Lightweight and broadband 2D MoS_2 nanosheets/3D carbon nanofibers hybrid aerogel for high-efficiency microwave absorption. *J Colloid Interface Sci* 2022;609:33-42. DOI PubMed
85. Zhou J, Qin J, Zhang X, et al. 2D space-confined synthesis of few-layer MoS_2 anchored on carbon nanosheet for lithium-ion battery anode. *ACS Nano* 2015;9:3837-48. DOI PubMed

86. Li L, Chen C, Su J, et al. Three-dimensional MoS_x ($1 < x < 2$) nanosheets decorated graphene aerogel for lithium-oxygen batteries. *J Mater Chem A* 2016;4:10986-91.
87. Yang M, Jeong J, Huh YS, Choi BG. High-performance supercapacitor based on three-dimensional MoS2/graphene aerogel composites. *Composites Science and Technology* 2015;121:123-8.
88. Gigot A, Fontana M, Serrapede M, et al. Mixed 1T-2H phase MoS_2/reduced graphene oxide as active electrode for enhanced supercapacitive performance. *ACS Appl Mater Interfaces* 2016;8:32842-52. DOI PubMed
89. Yuan J, Zhu J, Wang R, et al. 3D few-layered MoS_2/graphene hybrid aerogels on carbon fiber papers: a free-standing electrode for high-performance lithium/sodium-ion batteries. *Chemical Engineering Journal* 2020;398:125592.
90. Yuan Y, Lv H, Xu Q, Liu H, Wang Y. A few-layered MoS_2 nanosheets/nitrogen-doped graphene 3D aerogel as a high performance and long-term stability supercapacitor electrode. *Nanoscale* 2019;11:4318-27. DOI PubMed
91. Lee WS, Peng E, Loh TA, Huang X, Xue JM. Few-layer MoS_2-anchored graphene aerogel paper for free-standing electrode materials. *Nanoscale* 2016;8:8042-7. DOI PubMed
92. Wang S, Wang R, Zhao Q, et al. Freeze-drying induced self-assembly approach for scalable constructing MoS_2/graphene hybrid aerogels for lithium-ion batteries. *J Colloid Interface Sci* 2019;544:37-45. DOI PubMed
93. Das S, Ghosh R, Routh P, et al. Conductive MoS_2 quantum dot/polyaniline aerogel for enhanced electrocatalytic hydrogen evolution and photoresponse properties. *ACS Appl Nano Mater* 2018;1:2306-16. DOI
94. Zhang X, Nie Y, Zhang Q, Liang Z, Wang P, Ma Q. Polydopamine nanoparticles@MoS_2 nanosheet aerogel-based ECL sensing system for MiRNA-126 detection. *Chemical Engineering Journal* 2021;411:128428. DOI
95. Jaiswal MK, Carrow JK, Gentry JL, et al. Vacancy-Driven Gelation using defect-rich nanoassemblies of 2D transition metal dichalcogenides and polymeric binder for biomedical applications. *Adv Mater* 2017;29:1702037. DOI PubMed
96. Wang Q, Guo Q, Jia F, Li Y, Song S. Facile preparation of three-dimensional MoS_2 aerogels for highly efficient solar desalination. *ACS Appl Mater Interfaces* 2020;12:32673-80. DOI PubMed
97. Yang L, Mukhopadhyay A, Jiao Y, et al. Ultralight, highly thermally insulating and fire resistant aerogel by encapsulating cellulose nanofibers with two-dimensional MoS_2. *Nanoscale* 2017;9:11452-62. DOI PubMed
98. Cheng JB, Zhao HB, Cao M, et al. Banana leaflike C-doped MoS_2 aerogels toward excellent microwave absorption performance. *ACS Appl Mater Interfaces* 2020;12:26301-12. DOI PubMed
99. Jia F, Liu C, Yang B, et al. Thermal modification of the molybdenum disulfide surface for tremendous improvement of Hg^{2+} adsorption from aqueous solution. *ACS Sustainable Chem Eng* 2018;6:9065-73. DOI
100. Liu C, Kong D, Hsu PC, et al. Rapid water disinfection using vertically aligned MoS_2 nanofilms and visible light. *Nat Nanotechnol* 2016;11:1098-104. DOI PubMed
101. Yao K, Xu Z, Huang J, et al. Bundled defect-rich MoS_2 for a high-rate and long-life sodium-ion battery: achieving 3D diffusion of sodium ion by vacancies to improve kinetics. *Small* 2019;15:e1805405. DOI PubMed
102. Yang Z, Zhu L, Lv C, et al. Defect engineering of molybdenum disulfide for energy storage. *Mater Chem Front* 2021;5:5880-96. DOI
103. He Z, Zhao R, Chen X, et al. Defect engineering in single-layer MoS_2 using heavy ion irradiation. *ACS Appl Mater Interfaces* 2018;10:42524-33. DOI PubMed
104. Thiruraman JP, Fujisawa K, Danda G, et al. Angstrom-size defect creation and ionic transport through pores in single-layer MoS_2. *Nano Lett* 2018;18:1651-9. DOI PubMed
105. Zhao G, Deng H, Tyree N, et al. Recent Progress On Irradiation-Induced Defect Engineering Of Two-Dimensional 2H-MoS_2 few layers. *Applied Sciences* 2019;9:678. DOI
106. Mishra P, Tangi M, Ng TK, et al. Impact of N-plasma and Ga-irradiation on MoS_2 layer in molecular beam epitaxy. *Appl Phys Lett* 2017;110:012101.
107. Ochedowski O, Marinov K, Wilbs G, et al. Radiation hardness of graphene and MoS_2 field effect devices against swift heavy ion irradiation. *Journal of Applied Physics* 2013;113:214306.
108. Madauß L, Ochedowski O, Lebius H, et al. Defect engineering of single- and few-layer MoS_2 by swift heavy ion irradiation. *2D Mater* 2017;4:015034. DOI
109. Guo H, Sun Y, Zhai P, et al. Swift-heavy ion irradiation-induced latent tracks in few- and mono-layer MoS_2. *Appl Phys A* 2016:122. DOI
110. Mignuzzi S, Pollard AJ, Bonini N, et al. Effect of disorder on Raman scattering of single-layer MoS_2. *Phys Rev B* 2015:91.
111. Chen P, Ni J, Liang Y, Yang B, Jia F, Song S. Piezo-photocatalytic reduction of Au(I) by Defect-Rich MoS_2 nanoflowers for efficient gold recovery from a thiosulfate solution. *ACS Sustainable Chem Eng* 2021;9:589-98.
112. Jayabal S, Saranya G, Wu J, Liu Y, Geng D, Meng X. Understanding the high-electrocatalytic performance of two-dimensional MoS_2 nanosheets and their composite materials. *J Mater Chem A* 2017;5:24540-63.
113. Jia F, Liu C, Yang B, Song S. Microscale control of edge defect and oxidation on molybdenum disulfide through thermal treatment in air and nitrogen atmospheres. *Applied Surface Science* 2018;462:471-9.
114. Liu C, Wang Q, Jia F, Song S. Adsorption of heavy metals on molybdenum disulfide in water: a critical review. *Journal of Molecular Liquids* 2019;292:111390.
115. Yamamoto S, Kaneo Y, Maeda H. Styrene maleic acid anhydride copolymer (SMA) for the encapsulation of sparingly water-soluble drugs in nanoparticles. *Journal of Drug Delivery Science and Technology* 2013;23:231-7.

116. Zhou H, Yu F, Liu Y, et al. Thickness-dependent patterning of MoS_2 sheets with well-oriented triangular pits by heating in air. *Nano Res* 2013;6:703-11.
117. Jia F, Sun K, Yang B, Zhang X, Wang Q, Song S. Defect-rich molybdenum disulfide as electrode for enhanced capacitive deionization from water. *Desalination* 2018;446:21-30.
118. Jariwala D, Sangwan VK, Lauhon LJ, Marks TJ, Hersam MC. Emerging device applications for semiconducting two-dimensional transition metal dichalcogenides. *ACS Nano* 2014;8:1102-20. DOI PubMed
119. Behura S, Nguyen P, Che S, Debbarma R, Berry V. Large-area, transfer-free, oxide-assisted synthesis of hexagonal boron nitride films and their heterostructures with MoS_2 and WS_2. *J Am Chem Soc* 2015;137:13060-5. DOI PubMed
120. Jin H, Guo C, Liu X, et al. Emerging two-dimensional nanomaterials for electrocatalysis. *Chem Rev* 2018;118:6337-408. DOI PubMed
121. Luo P, Zhuge F, Zhang Q, et al. Doping engineering and functionalization of two-dimensional metal chalcogenides. *Nanoscale Horiz* 2019;4:26-51. DOI PubMed
122. Suh J, Park TE, Lin DY, et al. Doping against the native propensity of MoS_2: degenerate hole doping by cation substitution. *Nano Lett* 2014;14:6976-82. DOI PubMed
123. Tosun M, Chan L, Amani M, et al. Air-stable n-doping of WSe_2 by anion vacancy formation with mild plasma treatment. *ACS Nano* 2016;10:6853-60. DOI PubMed
124. Xu EZ, Liu HM, Park K, et al. p-Type transition-metal doping of large-area MoS_2 thin films grown by chemical vapor deposition. *Nanoscale* 2017;9:3576-84. DOI PubMed
125. Zhang K, Feng S, Wang J, et al. Manganese doping of monolayer MoS_2: the substrate is critical. *Nano Lett* 2015;15:6586-91. DOI PubMed
126. Wang J, Fang H, Wang X, Chen X, Lu W, Hu W. Recent progress on localized field enhanced two-dimensional material photodetectors from ultraviolet-visible to infrared. *Small* 2017;13:1700894. DOI PubMed
127. Lee S, Lee YT, Park SG, et al. Dimensional crossover transport induced by substitutional atomic doping in $SnSe_2$. *Adv Electron Mater* 2018;4:1700563. DOI
128. Yazdani S, Yarali M, Cha JJ. Recent progress on in situ characterizations of electrochemically intercalated transition metal dichalcogenides. *Nano Res* 2019;12:2126-39. DOI
129. Li Y, Cain JD, Hanson ED, et al. Au@MoS_2 core-shell heterostructures with strong light-matter interactions. *Nano Lett* 2016;16:7696-702. DOI PubMed
130. Kiriya D, Tosun M, Zhao P, Kang JS, Javey A. Air-stable surface charge transfer doping of MoS_2 by benzyl viologen. *J Am Chem Soc* 2014;136:7853-6. DOI PubMed
131. Zhan W, Yuan Y, Yao X, et al. Efficient recovery of gold(I) from thiosulfate solutions through photocatalytic reduction with Mn(II)-doped MoS_2. *ACS Sustainable Chem Eng* 2021;9:11681-90. DOI
132. Huo N, Konstantatos G. Ultrasensitive all-2D MoS_2 phototransistors enabled by an out-of-plane MoS_2 PN homojunction. *Nat Commun* 2017;8:572. DOI PubMed PMC
133. Li Y, Xu CY, Hu P, Zhen L. Carrier control of MoS_2 nanoflakes by functional self-assembled monolayers. *ACS Nano* 2013;7:7795-804. DOI PubMed
134. Fang H, Tosun M, Seol G, et al. Degenerate n-doping of few-layer transition metal dichalcogenides by potassium. *Nano Lett* 2013;13:1991-5. DOI PubMed
135. Chang YM, Yang SH, Lin CY, et al. Reversible and precisely controllable p/n-type doping of $MoTe_2$ transistors through electrothermal doping. *Adv Mater* 2018;30:e1706995. DOI PubMed
136. Tongay S. Preface to a special topic: 2D materials and applications. *Applied Physics Reviews* 2018;5:010401. DOI
137. Tongay S, Zhou J, Ataca C, et al. Broad-range modulation of light emission in two-dimensional semiconductors by molecular physisorption gating. *Nano Lett* 2013;13:2831-6. DOI PubMed
138. Nan H, Wang Z, Wang W, et al. Strong photoluminescence enhancement of $MoS(_2)$ through defect engineering and oxygen bonding. *ACS Nano* 2014;8:5738-45. DOI PubMed
139. Lei S, Wang X, Li B, et al. Surface functionalization of two-dimensional metal chalcogenides by Lewis acid-base chemistry. *Nat Nanotechnol* 2016;11:465-71. DOI PubMed
140. Cai L, McClellan CJ, Koh AL, et al. Rapid flame synthesis of atomically thin MoO_3 down to monolayer thickness for effective hole doping of WSe_2. *Nano Lett* 2017;17:3854-61. DOI PubMed
141. McDonnell S, Azcatl A, Addou R, et al. Hole contacts on transition metal dichalcogenides: interface chemistry and band alignments. *ACS Nano* 2014;8:6265-72. DOI PubMed
142. Sarkar D, Xie X, Kang J, et al. Functionalization of transition metal dichalcogenides with metallic nanoparticles: implications for doping and gas-sensing. *Nano Lett* 2015;15:2852-62. DOI PubMed
143. Javey A, Tu R, Farmer DB, Guo J, Gordon RG, Dai H. High performance n-type carbon nanotube field-effect transistors with chemically doped contacts. *Nano Lett* 2005;5:345-8. DOI PubMed
144. Roncali J. Molecular bulk heterojunctions: an emerging approach to organic solar cells. *Acc Chem Res* 2009;42:1719-30. DOI PubMed
145. Lin J, Zhong J, Zhong S, Li H, Zhang H, Chen W. Modulating electronic transport properties of MoS_2 field effect transistor by surface overlayers. *Appl Phys Lett* 2013;103:063109. DOI

146. Rai A, Valsaraj A, Movva HC, et al. Air stable doping and intrinsic mobility enhancement in monolayer molybdenum disulfide by amorphous titanium suboxide encapsulation. *Nano Lett* 2015;15:4329-36. DOI PubMed
147. Shi Y, Huang JK, Jin L, et al. Selective decoration of Au nanoparticles on monolayer MoS_2 single crystals. *Sci Rep* 2013;3:1839. DOI PubMed PMC
148. Du Y, Liu H, Neal AT, Si M, Ye PD. Molecular doping of multilayer MoS_2 field-effect transistors: reduction in sheet and contact resistances. *IEEE Electron Device Lett* 2013;34:1328-30. DOI
149. Dolui K, Rungger I, Das Pemmaraju C, Sanvito S. Possible doping strategies for MoS_2 monolayers: an. *ab initio* :88. DOI
150. Zhan W, Jia F, Yuan Y, et al. Controllable incorporation of oxygen in MoS_2 for efficient adsorption of Hg^{2+} in aqueous solutions. *J Hazard Mater* 2020;384:121382. DOI PubMed
151. Title RS, Shafer MW. Band structure of the layered transition-metal dichalcogenides: an experimental study by electron paramagnetic resonance on Nb-doped MoS_2. *Phys Rev Lett* 1972;28:808-10. DOI
152. Laskar MR, Nath DN, Ma L, et al. P-type doping of MoS_2 thin films using Nb. *Appl Phys Lett* 2014;104:092104. DOI
153. Gao J, Kim YD, Liang L, et al. Transition-metal substitution doping in synthetic atomically thin semiconductors. *Adv Mater* 2016;28:9735-43. DOI PubMed
154. Lin YC, Dumcenco DO, Komsa HP, et al. Properties of individual dopant atoms in single-layer MoS_2: atomic structure, migration, and enhanced reactivity. *Adv Mater* 2014;26:2857-61. DOI PubMed
155. Ramasubramaniam A, Naveh D. Mn-doped monolayer MoS_2: an atomically thin dilute magnetic semiconductor. *Phys Rev B* 2013:87. DOI
156. Li H, Duan X, Wu X, et al. Growth of alloy $MoS_{(2x)}Se_{2(1-x)}$ nanosheets with fully tunable chemical compositions and optical properties. *J Am Chem Soc* 2014;136:3756-9. DOI PubMed
157. Ma Q, Isarraraz M, Wang CS, et al. Postgrowth tuning of the bandgap of single-layer molybdenum disulfide films by sulfur/selenium exchange. *ACS Nano* 2014;8:4672-7. DOI PubMed
158. Zhou W, Hou D, Sang Y, et al. MoO_2 nanobelts@nitrogen self-doped MoS_2 nanosheets as effective electrocatalysts for hydrogen evolution reaction. *J Mater Chem A* 2014;2:11358. DOI
159. Qin S, Lei W, Liu D, Chen Y. In-situ and tunable nitrogen-doping of MoS_2 nanosheets. *Sci Rep* 2014;4:7582. DOI PubMed PMC
160. Chen M, Nam H, Wi S, et al. Stable few-layer MoS_2 rectifying diodes formed by plasma-assisted doping. *Appl Phys Lett* 2013;103:142110.
161. Nipane A, Karmakar D, Kaushik N, Karande S, Lodha S. Few-layer MoS_2 p-Type devices enabled by selective doping using low energy phosphorus implantation. *ACS Nano* 2016;10:2128-37. DOI PubMed
162. Wan J, Lacey SD, Dai J, Bao W, Fuhrer MS, Hu L. Tuning two-dimensional nanomaterials by intercalation: materials, properties and applications. *Chem Soc Rev* 2016;45:6742-65. DOI PubMed
163. Gao Y, Hu M, Mi B. Membrane surface modification with TiO_2-graphene oxide for enhanced photocatalytic performance. *Journal of Membrane Science* 2014;455:349-56.
164. Dumcenco D, Ovchinnikov D, Marinov K, et al. Large-area epitaxial monolayer MoS_2. *ACS Nano* 2015;9:4611-20. DOI PubMed PMC
165. Guo Y, Wei Y, Li H, Zhai T. Layer structured materials for advanced energy storage and conversion. *Small* 2017;13:1701649. DOI PubMed
166. Enyashin AN, Yadgarov L, Houben L, et al. New route for stabilization of 1T-WS_2 and MoS_2 phases. *J Phys Chem C* 2011;115:24586-91.
167. Lukowski MA, Daniel AS, Meng F, Forticaux A, Li L, Jin S. Enhanced hydrogen evolution catalysis from chemically exfoliated metallic MoS_2 nanosheets. *J Am Chem Soc* 2013;135:10274-7. DOI PubMed
168. Acerce M, Voiry D, Chhowalla M. Metallic 1T phase MoS_2 nanosheets as supercapacitor electrode materials. *Nat Nanotechnol* 2015;10:313-8. DOI PubMed
169. Gong Y, Yuan H, Wu CL, et al. Spatially controlled doping of two-dimensional SnS_2 through intercalation for electronics. *Nat Nanotechnol* 2018;13:294-9. DOI PubMed
170. Koski KJ, Wessells CD, Reed BW, Cha JJ, Kong D, Cui Y. Chemical intercalation of zerovalent metals into 2D layered Bi_2Se_3 nanoribbons. *J Am Chem Soc* 2012;134:13773-9. DOI PubMed
171. Chen KP, Chung FR, Wang M, Koski KJ. Dual element intercalation into 2D layered Bi_2Se_3 nanoribbons. *J Am Chem Soc* 2015;137:5431-7. DOI PubMed
172. Kumar P, Skomski R, Pushpa R. Magnetically ordered transition-metal-intercalated WSe_2. *ACS Omega* 2017;2:7985-90. DOI PubMed PMC
173. Morosan E, Zandbergen HW, Dennis BS, et al. Superconductivity in Cu_xTiSe_2. *Nature Phys* 2006;2:544-50. DOI PubMed
174. Chen Z, Leng K, Zhao X, et al. Interface confined hydrogen evolution reaction in zero valent metal nanoparticles-intercalated molybdenum disulfide. *Nat Commun* 2017;8:14548. DOI PubMed PMC
175. Yuwen L, Xu F, Xue B, et al. General synthesis of noble metal (Au, Ag, Pd, Pt) nanocrystal modified MoS_2 nanosheets and the enhanced catalytic activity of Pd-MoS_2 for methanol oxidation. *Nanoscale* 2014;6:5762-9. DOI PubMed
176. Sun K, Jia F, Yang B, Lin C, Li X, Song S. Synergistic effect in the reduction of Cr(VI) with Ag-MoS_2 as photocatalyst. *Applied Materials Today* 2020;18:100453. DOI
177. Guo M, Xing Z, Zhao T, et al. Hollow flower-like polyhedral α-Fe_2O_3/Defective MoS_2/Ag Z-scheme heterojunctions with enhanced

photocatalytic-Fenton performance via surface plasmon resonance and photothermal effects. *Applied Catalysis B: Environmental* 2020;272:118978. DOI

178. Yin Z, Chen B, Bosman M, et al. Au nanoparticle-modified MoS_2 nanosheet-based photoelectrochemical cells for water splitting. *Small* 2014;10:3537-43. DOI PubMed
179. Luo Y, Huang D, Li M, et al. MoS_2 nanosheet decorated with trace loads of Pt as highly active electrocatalyst for hydrogen evolution reaction. *Electrochimica Acta* 2016;219:187-93. DOI
180. Sun W, Wang J, Wang K, et al. Turbulence-like Cu/MoS_2 films: structure, mechanical and tribological properties. *Surface and Coatings Technology* 2021;422:127490. DOI
181. Lan S, Jing B, Yu C, et al. Protrudent iron single-atom accelerated interfacial piezoelectric polarization for self-powered water motion triggered fenton-like reaction. *Small* 2022;18:e2105279. DOI PubMed
182. He X, Wu P, Wang S, Wang A, Wang C, Ding P. Inactivation of harmful algae using photocatalysts: Mechanisms and performance. *Journal of Cleaner Production* 2021;289:125755.
183. Yang X, Chen Z, Zhao W, et al. Recent advances in photodegradation of antibiotic residues in water. *Chem Eng J* 2021;405:126806. DOI PubMed PMC
184. Zhan W, Yuan Y, Yang B, Jia F, Song S. Construction of MoS_2 nano-heterojunction via ZnS doping for enhancing in-situ photocatalytic reduction of gold thiosulfate complex. *Chemical Engineering Journal* 2020;394:124866.
185. Marschall R. Semiconductor composites: strategies for enhancing charge carrier separation to improve photocatalytic activity. *Adv Funct Mater* 2014;24:2421-40.
186. Zhou H, Qu Y, Zeid T, Duan X. Towards highly efficient photocatalysts using semiconductor nanoarchitectures. *Energy Environ Sci* 2012;5:6732.
187. Lu L, Wu B, Shi W, Cheng P. Metal-organic framework-derived heterojunctions as nanocatalysts for photocatalytic hydrogen production. *Inorg Chem Front* 2019;6:3456-67.
188. Ma S, Xie J, Wen J, et al. Constructing 2D layered hybrid CdS nanosheets/MoS_2 heterojunctions for enhanced visible-light photocatalytic H_2 generation. *Applied Surface Science* 2017;391:580-91. DOI
189. Lu X, Jin Y, Zhang X, et al. Controllable synthesis of graphitic C_3N_4/ultrathin MoS_2 nanosheet hybrid nanostructures with enhanced photocatalytic performance. *Dalton Trans* 2016;45:15406-14. DOI PubMed
190. He M, Sun K, Suryawanshi MP, Li J, Hao X. Interface engineering of p-n heterojunction for kesterite photovoltaics: a progress review. *Journal of Energy Chemistry* 2021;60:1-8. DOI
191. Low J, Yu J, Jaroniec M, Wageh S, Al-Ghamdi AA. Heterojunction photocatalysts. *Adv Mater* 2017;29:1601694. DOI PubMed
192. Yu W, Zhang S, Chen J, et al. Biomimetic Z-scheme photocatalyst with a tandem solid-state electron flow catalyzing H_2 evolution. *J Mater Chem A* 2018;6:15668-74.
193. Low J, Dai B, Tong T, Jiang C, Yu J. In situ irradiated x-ray photoelectron spectroscopy investigation on a direct z-scheme TiO_2 /CdS composite film photocatalyst. *Adv Mater* 2019;31:e1802981.
194. Qi K, Cheng B, Yu J, Ho W. A review on TiO_2 -based Z-scheme photocatalysts. *Chinese Journal of Catalysis* 2017;38:1936-55. DOI PubMed PMC
195. Ani I, Akpan U, Olutoye M, Hameed B. Photocatalytic degradation of pollutants in petroleum refinery wastewater by TiO_2- and ZnO-based photocatalysts: Recent development. *Journal of Cleaner Production* 2018;205:930-54.
196. Xiong T, Wen M, Dong F, et al. Three dimensional Z-scheme $(BiO)_2CO_3$/MoS_2 with enhanced visible light photocatalytic NO removal. *Applied Catalysis B: Environmental* 2016;199:87-95. DOI
197. Zhang W, Xiao X, Li Y, Zeng X, Zheng L, Wan C. Liquid-exfoliation of layered MoS_2 for enhancing photocatalytic activity of TiO_2 /g-C_3N_4 photocatalyst and DFT study. *Applied Surface Science* 2016;389:496-506. DOI
198. Fu J, Xu Q, Low J, Jiang C, Yu J. Ultrathin 2D/2D WO_3/g-C_3N_4 step-scheme H_2-production photocatalyst. *Applied Catalysis B: Environmental* 2019;243:556-65. DOI
199. He F, Meng A, Cheng B, Ho W, Yu J. Enhanced photocatalytic H_2-production activity of WO_3/TiO_2 step-scheme heterojunction by graphene modification. *Chinese Journal of Catalysis* 2020;41:9-20. DOI
200. Xu Q, Zhang L, Cheng B, Fan J, Yu J. S-scheme heterojunction photocatalyst. *Chem* 2020;6:1543-59. DOI
201. He X, Wang A, Wu P, et al. Photocatalytic degradation of microcystin-LR by modified TiO_2 photocatalysis: a review. *Sci Total Environ* 2020;743:140694. DOI PubMed
202. Alshamsi HA, Beshkar F, Amiri O, Salavati-Niasari M. Porous hollow Ag/Ag_2S/Ag_3PO_4 nanocomposites as highly efficient heterojunction photocatalysts for the removal of antibiotics under simulated sunlight irradiation. *Chemosphere* 2021;274:129765. DOI PubMed
203. Fan H, Zhou H, Li W, Gu S, Zhou G. Facile fabrication of 2D/2D step-scheme In_2S_3/$Bi_2O_2CO_3$ heterojunction towards enhanced photocatalytic activity. *Applied Surface Science* 2020;504:144351. DOI
204. Bartolomeo A. Graphene schottky diodes: an experimental review of the rectifying graphene/semiconductor heterojunction. *Physics Reports* 2016;606:1-58. DOI
205. Sajan CP, Wageh S, Al-ghamdi AA, Yu J, Cao S. TiO_2 nanosheets with exposed {001} facets for photocatalytic applications. *Nano Res* 2016;9:3-27. DOI
206. Yu J, Low J, Xiao W, Zhou P, Jaroniec M. Enhanced photocatalytic CO_2-reduction activity of anatase TiO_2 by coexposed {001} and {101} facets. *J Am Chem Soc* 2014;136:8839-42. DOI PubMed

207. Zhou K, Li Y. Catalysis based on nanocrystals with well-defined facets. *Angew Chem Int Ed Engl* 2012;51:602-13. DOI PubMed
208. Zhang X, Jia F, Yang B, Song S. Oxidation of molybdenum disulfide sheet in water under in situ atomic force microscopy observation. *J Phys Chem C* 2017;121:9938-43. DOI
209. Zafar F, Wang H, Lv C, et al. Enhancement of GAD storage stability with immobilization on PDA-coated superparamagnetic magnetite nanoparticles. *Catalysts* 2019;9:969. DOI
210. Wang Y, Zeng S, Sun K, Yang B, Jia F, Song S. Wang Y, Zeng S, Sun K, Yang B, Jia F, Song S. Highly stable MoS_2@PDA composite for enhanced reduction of $AuCl_4^-$. *Chemical Physics Letters* 2020;747:137350. DOI
211. Sun K, Mao S, Zhan W, Liu C, Jia F, Song S. In-situ reduction of $Au(S_2O_3)_2^{3-}$ for efficient recovery of gold with magnetically separable shell-core structured MoS_2@Fe_3O_4 composite. *Hydrometallurgy* 2020;198:105514. DOI
212. Wang Q, Peng L, Gong Y, Jia F, Song S, Li Y. Mussel-inspired Fe_3O_4@polydopamine(PDA)-MoS_2 core-shell nanosphere as a promising adsorbent for removal of Pb^{2+} from water. *Journal of Molecular Liquids* 2019;282:598-605. DOI